Biophysical Journal
Article

Biophysical Society

Decoding Calcium Signaling Dynamics during *Drosophila* Wing Disc Development

Pavel A. Brodskiy,[1] Qinfeng Wu,[1] Dharsan K. Soundarrajan,[1] Francisco J. Huizar,[1] Jianxu Chen,[2] Peixian Liang,[2] Cody Narciso,[1] Megan K. Levis,[1] Ninfamaria Arredondo-Walsh,[1] Danny Z. Chen,[2] and Jeremiah J. Zartman[1,*]
[1]Department of Chemical and Biomolecular Engineering and [2]Department of Computer Science and Engineering, University of Notre Dame, Notre Dame, Indiana

ABSTRACT The robust specification of organ development depends on coordinated cell-cell communication. This process requires signal integration among multiple pathways, relying on second messengers such as calcium ions. Calcium signaling encodes a significant portion of the cellular state by regulating transcription factors, enzymes, and cytoskeletal proteins. However, the relationships between the inputs specifying cell and organ development, calcium signaling dynamics, and final organ morphology are poorly understood. Here, we have designed a quantitative image-analysis pipeline for decoding organ-level calcium signaling. With this pipeline, we extracted spatiotemporal features of calcium signaling dynamics during the development of the *Drosophila* larval wing disc, a genetic model for organogenesis. We identified specific classes of wing phenotypes that resulted from calcium signaling pathway perturbations, including defects in gross morphology, vein differentiation, and overall size. We found four qualitative classes of calcium signaling activity. These classes can be ordered based on agonist stimulation strength Gαq-mediated signaling. In vivo calcium signaling dynamics depend on both receptor tyrosine kinase/phospholipase C γ and G protein-coupled receptor/phospholipase C β activities. We found that spatially patterned calcium dynamics correlate with known differential growth rates between anterior and posterior compartments. Integrated calcium signaling activity decreases with increasing tissue size, and it responds to morphogenetic perturbations that impact organ growth. Together, these findings define how calcium signaling dynamics integrate upstream inputs to mediate multiple response outputs in developing epithelial organs.

INTRODUCTION

Organ development requires the coordination of many cells to form a structurally integrated tissue. Important properties of the final organ architecture include its shape, size, and spatial distribution of cell types. Notably, the information processing network required for development resembles a "bow-tie" network structure with many input signals that are funneled through a limited number of second messengers (1–3) (Fig. 1 *A*). Signal integration and pathway crosstalk result in many possible downstream outputs that are determined by effector proteins that regulate cellular processes, including cell division, migration, mechanical properties, death, and cell differentiation state (1). However, how these diverse input signals regulate the dynamics of second messengers is poorly understood. Further, how organ-level properties, such as size and shape, emerge from the integration of second messenger signaling remains to be fully elucidated.

A key second messenger that serves as a central node in the bow-tie structure is the calcium ion (Ca^{2+}) (4). Ca^{2+} signaling is a ubiquitous transducer of cellular information and plays key roles in regulating cell behaviors, such as cell division, growth, and death (5). Ca^{2+} dynamics regulate cellular properties and behavior during animal development, and perturbations to Ca^{2+} signaling often lead to disease (3,6–16). Cells can encode complex signals into a Ca^{2+} signaling "signature," which includes amplitude, frequency, and integrated intensity of Ca^{2+} oscillations (13,17). Cells decode these signaling signatures by modulating the activities of downstream enzymes and transcription factors (Fig. 1 *A*).

Intercellular Ca^{2+} signaling is correlated with many developmental processes. For example, they have been found to regulate scale development in the butterfly (18). Ca^{2+} waves are indispensable to activate *Drosophila* egg development (19), and Ca^{2+} spikes are important for development of *Drosophila* and *Xenopus* embryos (8,11,16,20,21). Ca^{2+} signaling responds to Hedgehog (Hh) signaling in the frog

Submitted August 17, 2018, and accepted for publication January 4, 2019.
*Correspondence: jzartman@nd.edu
Pavel A. Brodskiy and Qinfeng Wu contributed equally to this work.
Editor: Stanislav Shvartsman.
https://doi.org/10.1016/j.bpj.2019.01.007

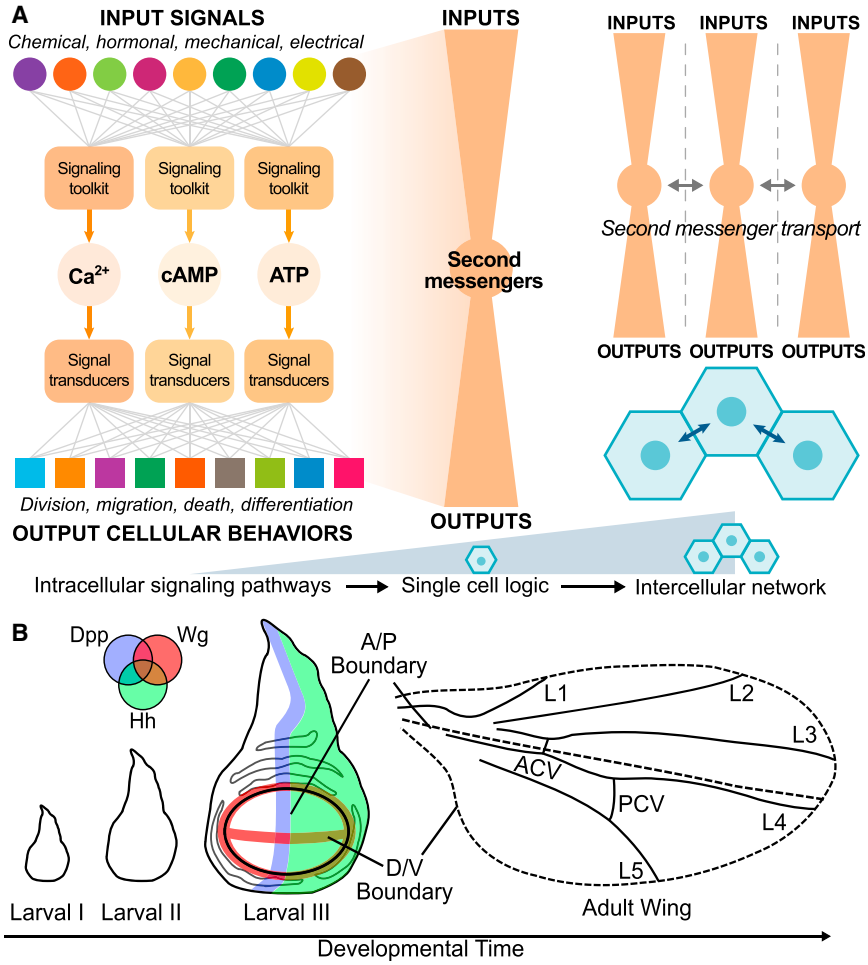

FIGURE 1 The wing disc as a model system of signal integration during organogenesis. (*A*) Second messengers are central nodes of a bow-tie structure that integrates various input signals to inform cellular behaviors. The information from a coupled intercellular network results in emergent tissue-scale phenomena. (*B*) Schematic describing the development of the *Drosophila* wing from the wing disc is shown. The wing disc grows rapidly during larval stages and develops into the adult wing. Spatial patterning of cell fates is determined by the combined actions of morphogenetic signals, including Hedgehog (Hh), BMP/Decapentaplegic (Dpp), and Wnt/Wingless (Wg). After larval growth, the wing disc undergoes morphogenesis to form the wing and the thorax. The larval pouch is approximately an oval. The pouch cells later form the wing blade. In the adult wing, there are L1–L5 veins, anterior crossvein (ACV), and posterior crossvein (PCV). This study focuses on Ca^{2+} signaling dynamics in the third instar wing disc pouch, after primary patterning of anterior/posterior and dorsal/ventral compartments has occurred. To see this figure in color, go online.

neural cord (22), correlates with Decapentaplegic (Dpp) secretion in *Drosophila* imaginal discs (23), and is indispensable for human neural rosette development (24). Ca^{2+} dynamics also are essential for cell migration and tissue contractility in zebrafish, Japanese newt, and chick embryos (9,20,25). Recently, intercellular Ca^{2+} transients (ICTs) have been observed in the *Drosophila* wing disc, both in vivo and ex vivo (15,26–28), and have been implicated as a first response to wounding (27) and robustness in regeneration (15), tissue homeostasis (26), and mechanotransduction (15,29). Inhibition of Ca^{2+} significantly also rescues cancerous overgrowth of wings, thus showing its regulatory role in tissue growth (30). However, a quantitative characterization of Ca^{2+} dynamics in organ development is lacking, in part because of a lack of image-processing methods and a suitable model system to analyze the stochastic nature of the signals. Consequently, there is a need for a systems-level description of Ca^{2+} signaling dynamics to decode the role of Ca^{2+} signaling in organ development.

The *Drosophila* wing imaginal disc pouch is a premier model system to study how epithelial cells undergo specific morphogenetic steps to form the intricate structure of an adult wing (31–36) (Fig. 1 *B*). The wing disc is a powerful model system because of the availability of tools to perturb gene expression in a specific region of a tissue (37). Multiple conserved regulatory modules for tissue development have been discovered in the wing disc. In the larval organ, morphogens divide the wing disc pouch into regions that define the differentiation state of cells and coordinate morphogenesis (Fig. 1 *B*). Morphogen signals that are important for wing disc development include Hh (reviewed in (38)) and Dpp (35,39), which define the anterior/posterior axis. Wg (reviewed in (40)) patterns the dorsal/ventral axis. Widely available genetic tools and simple geometry make the *Drosophila* wing disc a powerful platform to decode Ca^{2+} signaling at the systems level.

Here, we have developed an image-processing pipeline to quantitatively investigate the relationships between Ca^{2+} signaling and organ size. We first genetically inhibited key components of the core Ca^{2+} signaling pathway, termed elsewhere as the "Ca^{2+} signaling toolkit" (5), to define the range of adult wing phenotypes. Next, we performed a dose-response experiment of fly extract (FEX) to order the

specific classes of Ca^{2+} signaling based on the relative concentration of agonist-based stimulation. We use the term "Ca^{2+} signaling activity" to collectively refer to these four Ca^{2+} signaling classes. We investigated how these classes of Ca^{2+} signaling correlate with disc age and size, both in vivo and ex vivo. We established that FEX stimulates Ca^{2+} through Gαq/phospholipase C (PLC) β signaling through genetic perturbation experiments. Next, we developed advanced image-analysis tools to handle the large data sets to extract quantitative Ca^{2+} dynamics measurements. Using this image-analysis pipeline, we identified a negative power-law correlation between integrated Ca^{2+} signaling activity and wing disc pouch size. We examined how the genetic state of the tissue modulates Ca^{2+} signaling dynamics through genetic perturbation. Ca^{2+} signaling activity responds to perturbations that impact the morphogenic state of the tissue, resulting in deviations from the quantitative correlation curve between Ca^{2+} signaling activity and developmental progression. Together, these trends indicate that Ca^{2+} signaling provides a biochemical readout of organ size. The results suggest Ca^{2+} could be involved in modulating cell proliferation activity during larval growth. In sum, this study provides significant evidence that Ca^{2+} signaling contributes to intercellular consensus-building during organ development (41). This research paves the road of revealing the quantitative and mechanistic regulation of organ development by Ca^{2+} signaling in future studies.

MATERIALS AND METHODS

Fly strains and genetics

Phenotypic analysis in Fig. 2 was performed using the MS1096-Gal4 line (BL#8860). A *nub > GCaMP6f* reporter tester line was used to measure relative Ca^{2+} signals in the wing disc pouch (29,42). Gene perturbations were generated by crossing the tester line to either RNA interference

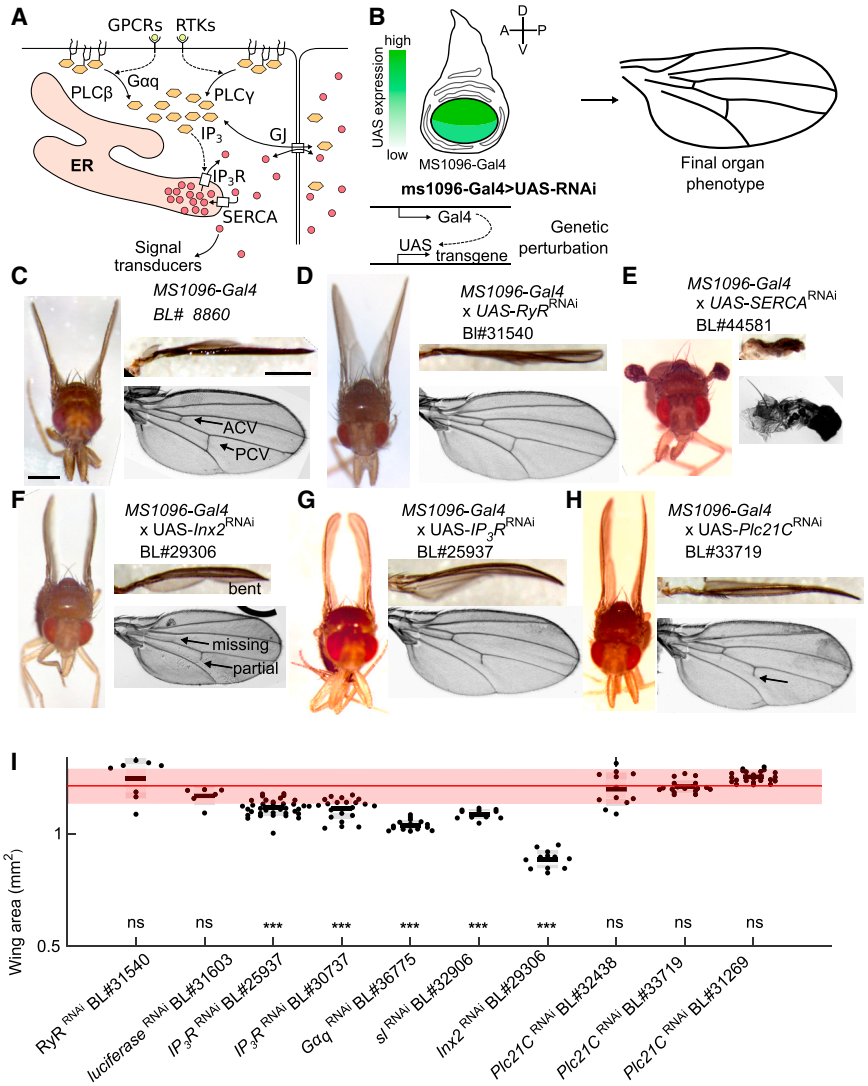

FIGURE 2 Core calcium signaling components modulate wing size, shape, and vein differentiation. (*A*) Schematic representing mechanism of the core IP_3R-mediated Ca^{2+} signaling pathway is shown. ER, endoplasmic reticulum; Gαq, G protein α q subunit; GJ, gap junction; GPCR, G protein-coupled receptor; IP_3, inositol trisphosphate; IP_3R, IP_3 receptor; PLC, phospholipase C, which includes multiple isoforms: PLCγ homolog (sl) and PLCβ homologs (Plc21C and norpA); RTK, receptor tyrosine kinase; SERCA, sarco/endoplasmic reticulum Ca^{2+}-ATPase. (*B*) Schematic of expression pattern of MS1096-Gal4, which is expressed more strongly in the dorsal compartment, is shown. The GAL4/UAS system was used to express RNAi constructs starting during the third instar larval stage. Adult wing phenotypes were used to provide a readout of final phenotype. (*C–H*) Micrographs of adult fly, orthogonal view of wing, and mounted view of wing for indicated crosses are shown. Scale bars represent 0.5 mm. (*I*) Total area of adult wings under various perturbations of Ca^{2+} signaling genes driven by MS1096-Gal4. The gray boxes indicate standard deviation. ns, not significant. $*p < 0.05$; $***p < 0.001$ by *t*-test after Bonferroni correction. The red band provides the average and SD of multiple control crosses. To see this figure in color, go online.

(RNAi)-based transgenic lines (UAS-*Gene* X^{RNAi}) or gene overexpression lines (UAS-*Gene X*). When possible, multiple independent RNAi lines were tested for each gene investigated. As a second round of controls, the tester line was also crossed to *UAS-mCherry* to obtain ratiometric measurements (Fig. S6). Validation of Ca^{2+}-based RNAi lines is reported in the Supporting Materials and Methods, Section 5 and in (29). Further details on genetic crosses and validation are detailed in the Supporting Materials and Methods.

In vivo imaging setup

Wandering third instar larvae were collected for imaging and rinsed in deionized water. Larvae were dried and then adhered to a coverslip for imaging with Scotch tape covering the larvae. The larvae were attached with their spiracles facing toward the coverslip to align the wing discs toward the microscope. The larvae were imaged at 20× magnification for 20 min on an EVOS FL Auto microscope (Thermo Fisher Scientific, Waltham, MA). Images were taken every 15 s.

Organ culture media

Organ culture studies were performed as detailed in (29,43) with modifications. We used 15% FEX for genetic perturbation studies performed ex vivo because it improved the signal/noise ratio for reliable quantification of Ca^{2+} dynamics, although there was more activity than in vivo measurements. ZB media +15% FEX contains 79.4% (v/v) ZB media (44), 0.6% (v/v) of 1 mg/mL insulin (Sigma-Aldrich, St. Louis, MO), 15% (v/v) ZB-based FEX, and 5% penicillin/streptomycin (Gibco, Carlsbad, CA). ZB media was developed as a chemically defined media to support *Drosophila* cell culture (44) and was used as the basal media for all experiments. The text of Supporting Materials and Methods provides details of FEX preparation.

Wing disc imaging setup

Wing discs were dissected from third instar larvae, cultured, and imaged as detailed in the Supporting Materials and Methods. All experiments were performed immediately after dissection to minimize the time in culture. Discs were imaged at three *z*-planes with a step size of 10 μm and 20× magnification and 10 s intervals for a total period of 1 h, with 200 ms exposure time and 50 mW 488 nm laser exposure at 44–70% laser intensity (Fig. S5). For some experiments, mCherry signal was imaged with a 560 nm laser (50% laser intensity).

Ex vivo data preprocessing

Microscopy resulted in four-dimensional time-lapse data (512 pixels by 512 pixels by three z-planes by 361 time points). The *z*-stack data was max-projected in FIJI (45) to yield *z*-projected time-lapse videos. Time points were selected so that discs were only analyzed during times in which disks did not move in the *z*-direction, with the shortest time lapse analyzed being 20 min.

Image segmentation and registration

For the image frame at each time point, a region of interest (ROI) defining the pouch was obtained using a novel deep-learning-based segmentation algorithm that we developed and is described in (46). Each frame was segmented with a fully convolutional network (FCN) module, and the ROI boundaries were refined by a graph-search algorithm. The FCN module was trained on 800 images of wing discs expressing *nub-GCaMP6f* with various stages of Ca^{2+} signaling activity. B-spline-based registration was used to transform image frames onto a shape defined by the first time point. The pipeline ensures that coordinates within the pouch are consistent from frame to frame, allowing spatial analysis of Ca^{2+} signatures.

The FCN was used to segment only the pouch region, excluding the *nub*-expressing hinge region dorsal to the pouch. Note that the traditional image segmentation methods explored could not distinguish well between these two types of regions. For data that had both a GCaMP6f and RFP channel, Rigid Registration was used in FIJI (45), as the RFP channel does not exhibit oscillatory dynamics.

Identification of the axes

The posterior and D compartments were identified manually based on the characteristic shapes of the pouch (Figs. 1 *B* and S1). Pouches were flipped so that the A compartment was on the left and the D compartment was on the top. A custom MATLAB (The MathWorks, Natick, MA) graphical user interface was used to reduce error in manual pouch orientation (Fig. S2). The graphical user interface also helped to reduce error in the manual pouch orientation. Details are found in Supporting Materials and Methods and Fig. S2.

Feature extraction

Images of each wing disc pouch were divided into square ROIs of 2.8 μm. We obtained time-averaged Ca^{2+} signatures for each ROI and represented them as a spatial map (see Fig. 6 *D*). Each set of spatial maps was averaged to obtain a composite spatial map for each feature. The Ca^{2+} signatures include amplitude, frequency, and integrated intensity. The Ca^{2+} signature was extracted by taking average intensity (F(t)) from 4 × 4 pixel (2.8 × 2.8 μm) spatial bins arrayed with square packing across the segmented disc pouch (Fig. S1, *A–C*). Video durations ranged from 20 to 60 min. Further details are included in the Supporting Materials and Methods Text and Figs. S1 and S2.

Qualitative analysis

The in vivo data were analyzed blindly and qualitatively by dividing each video into 135-s-clip segments and scoring them in random order. Ca^{2+} signaling activity in each segment was manually classified into one of the four previously mentioned categories. One sample may, in this way, be classified in multiple bins for the full video. Each clip was classified as having either no activity exceeding basal levels, cellular spikes, ICTs, intercellular Ca^{2+} waves (ICWs), fluttering, or being unanalyzable because of larval motion. If a time-lapse segment includes two or more categories, the most active category was annotated. This was done with a custom MATLAB script that divided each video into clips. One random clip was looped at a time until all the data had been classified. Afterwards, the fraction of time spent in each class was reported for each condition. Additional procedural details are included in the Supporting Materials and Methods.

Statistical analysis and visualization

The median value of each summary statistic for each ROI in each disc was compared across genetic conditions, pouch sizes, and between compartments (Fig. 6). ROIs within two spatial bins of the edge were excluded from the median to avoid edge effects. A two-tailed, unpaired, Student's *t*-test was performed in comparisons across conditions. The visualization of the manifold identified in Fig. 8 is a multivariate kernel density estimate with a cutoff value selected to display a three-dimensional region that encompasses a uniform density of measurements. As discussed in the Supporting Materials and Methods, this was done to clarify the manifold along which developing wing discs lie in the "morphological cell signaling" space.

RESULTS

The core calcium signaling pathway regulates final wing size, shape, and patterning robustness

The regulation of cytosolic Ca^{2+} levels occurs by regulating fluxes of Ca^{2+} between Ca^{2+} stores, such as the endoplasmic reticulum, and the cytosol (Fig. 2 *A*). We knocked down genes known to regulate Ca^{2+} signaling dynamics and characterized final wing morphologies as an initial step to systematically identify phenotypic outputs. We used *MS1096-Gal4* to express RNAi. *MS1096-Gal4* is expressed in the wing pouch, the precursor of the wing blade, and has stronger expression in the dorsal than the ventral compartment (Fig. 2 *B*; (47,48)). The parental *MS1096-Gal4* line was crossed to control lines such as UAS-RyR^{RNAi} (where RYR is not expected to have significant expression (49)) or other UAS-RNAi constructs that do not target endogenous messenger RNA (such as luc^{RNAi}). These did not exhibit significant morphological or size defects (Fig. 2, *C* and *D*).

Based on the wealth of literature on wing development, adult wing phenotypes provide important functional information into the downstream outputs of calcium signaling. We found that there are four major categories of wing defects in adult wings when perturbing Ca^{2+} signaling genes: 1) crumpling and blistering (Fig. 2 *E*), 2) wing bending (Fig. 2, *F–H*), 3) loss of crossveins and other vein defects (Fig. S11), and 4) reduction in wing size. *MS1096* > $SERCA^{RNAi}$ led to a severe shriveled wing (Fig. 2 *E*) (15,26). Knocking down gap junctions through *MS1096* > $Inx2^{RNAi}$ (RNAi phenotype for line is described in Pézier et al. (50); see Table S1) led to significantly smaller wings with defects, including partial loss, total loss, and deviation in the posterior crossvein (PCV) and anterior crossvein (Fig. 2, *F* and *I*). We observed that partial loss of the PCV was always the loss of the posterior side of the PCV and never the anterior side (n = 33). *MS1096* > IP_3R^{RNAi} exhibited similar wing defects (Fig. 2, *G* and *I*). The loss of crossveins is consistent with Ca^{2+} signaling playing a role in the secretion of growth and patterning molecules, such as Dpp (23). Earlier reports have also implicated Ca^{2+} signaling genes (including *Stim* and *Orai*) in vein patterning (26,51).

Notably, wing size was also significantly reduced for RNAi knockdowns to many of the core Ca^{2+} signaling components. *MS1096* > $Inx2^{RNAi}$ (Fig. 2 *I*), *MS1096* > IP_3R^{RNAi} (Fig. 2 *G*), and *MS1096* > $G\alpha q^{RNAi}$ (data not shown) wings are all bent and show a significant reduction of wing size. If a certain gene regulates growth, the asymmetric perturbation by *MS1096-Gal4* could lead to a differential reduction of dorsal and ventral wing area. This differential reduction of area could lead to bending of the final wing, which is formed by apposition of the dorsal and ventral compartments during pupal morphogenesis (Fig. 2, *C–G*). Together, these results demonstrate that Ca^{2+} signaling plays important roles in wing morphogenesis, vein patterning, and growth control.

Three homologs of the PLC family are present in *Drosophila*. *Plc21C* (PLCβ1) and *norpA* (PLCβ4) are stimulated by G protein-coupled receptors (GPCRs), and *sl* (PLCγ) is stimulated by receptor tyrosine kinases (RTKs), such as insulin receptor and epidermal growth factor receptor (52). We observed that *MS1096* > $Plc21C^{RNAi}$ wings had a similar bent wing phenotype and defects in crossvein patterning compared to the *MS1096* > IP_3R^{RNAi} and *MS1096* > $Inx2^{RNAi}$ wings, but did not have the same wing size phenotypes (Figs. 2, *H* and *I* and S9). *MS1096* > *norpA* also did not cause significant size phenotype (data not shown). An explanation for the weaker defect of *MS1096* > $Plc21C^{RNAi}$ compared to knockdown of IP_3R or $G\alpha q$ could be that it is caused by incomplete knockdown for the given RNAi lines tested or redundancy between PLCβ homologs. Another possibility is that the bent wing phenotype arises from defects in the mechanical regulation of cells during morphogenesis and is a separate phenotype from growth regulation. Previously, *sl* has been shown to modulate wing size (53), which is in agreement with our results (Fig. 2 *I*).

Taken together, these results show that IP_3R-mediated Ca^{2+} signaling contributes to multiple aspects of wing morphogenesis. Here, we have established that Ca^{2+} plays an important role in wing size control. These observations propelled us to investigate further the interplay and correlation between Ca^{2+} signaling dynamics and larval wing disc size, which is the stage of development governing overall organ growth as reviewed in (34,54).

Varying agonist concentration results in four ordinal classes of calcium signaling activity ex vivo

Previously, FEX has been reported to stimulate Ca^{2+} activity by our group and others (15,26,28,29). We first tested whether the extent of Ca^{2+} signaling exhibits a concentration dependence on FEX. To do so, we performed ex vivo imaging of Ca^{2+} signaling activity in the wing disc pouch using a genetically encoded Ca^{2+} sensor (*nub* > *GCaMP6f*). Wing discs were cultured with variable concentrations of FEX. We observed a consistent progression of four classes of Ca^{2+} signaling activity as the concentration of FEX increased (Fig. 3, *A–E*): 1) local Ca^{2+} spikes that occur in single cells (0% v/v FEX, Fig. 3 *A* and *A′*; Video S14); 2) stochastic, short-distance ICTs (2.5% v/v FEX, Fig. 3, *B* and *B′*; Video S15); 3) oscillatory long-range ICTs that we term ICWs (5–20% v/v FEX, Fig. 3, *C* and *C′*; Videos S16, S17, and S18); and 4) elevated cytoplasmic Ca^{2+} exhibiting rapid, low-amplitude oscillations that we term "fluttering" (40% v/v FEX, Fig. 3, *D*and *D′*; Video S19). Because the observed Ca^{2+} activity classes depend on the dose of FEX, we established the Ca^{2+} signaling activity to be ordinal, with spikes being the least active and fluttering being the most active. These results suggest that transitions

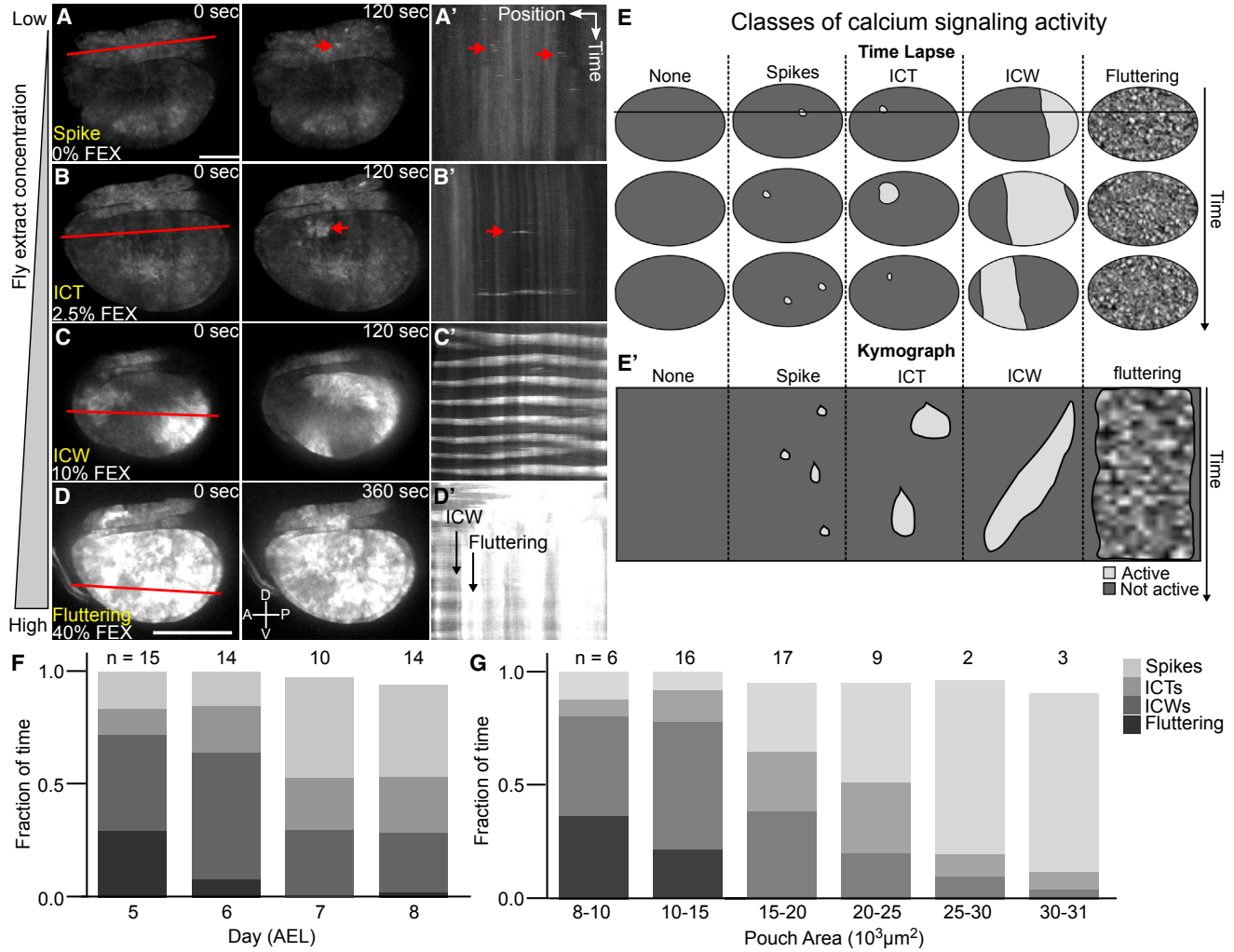

FIGURE 3 Increased stimulation of calcium signaling results in a progression of signaling classes. Wing discs were cultured in chemically defined ZB media with varying concentrations of fly extract (FEX): (*A*) 0%, (*B*) 2.5%, (*C*) 10%, and (*D*) 40% v/v FEX. These conditions stimulate four classes of Ca^{2+} signaling activity: spikes, ICTs, ICWs, and "fluttering" Ca^{2+} oscillations (Videos S14, S15, S16, S17, S18, and S19). (*A–D*) Montages from ex vivo time-lapse videos are shown. (*A′–D′*) Kymographs of the corresponding time-lapse videos along the indicated red lines are shown. Note: the kymograph slice in A was selected in the hinge region to clearly indicate examples of spikes. (*E*) Schematic of four classes of Ca^{2+} signaling activity is shown. The horizontal line represents the *x-y* position of the kymograph. (*E′*) Schematic representation of kymographs taken from (*E*) is shown. (*F* and *G*) Average fraction of time in each class of Ca^{2+} signaling activity for 15% FEX varies by (*F*) pouch age and (*G*) pouch size. Wing disks are oriented with anterior to the left and dorsal compartment to the top. AEL indicates days after egg laying. Position and timescale bars, 25 μm and 15 min. For (*F* and *G*), $p < 0.001$ for ordinal logistic regression model versus constant model. n indicates the sample size. To see this figure in color, go online.

in Ca^{2+} activity occur as the overall level of IP_3R-based signaling increases.

Next, we quantified the percentage of each class of Ca^{2+} signaling activity in wing discs of different ages and sizes throughout development while keeping the FEX concentration constant at 15%. The highest activity observed within each time segment established the annotated signaling class. For example, if ICTs and ICWs occur in the same time within the pouch, we characterized that fraction of time as ICW activity. We found that the occurrence of the highest Ca^{2+} signaling activities (ICWs and fluttering) decreased from 72% at 5 days after egg laying (AEL) to 29% at 8 days AEL (Fig. 3 *F*). Also, the occurrence of the highest Ca^{2+} signaling activity deceased from 80% in small pouches ($<8 \times 10^3$ μm^2) to 5% in large pouches ($>30 \times 10^3$ μm^2, Fig. 3 *G*). Importantly, our observations demonstrate that ex vivo Ca^{2+} signaling activity in 15% FEX correlates strongly with both the age of the larvae and the size of the wing disc pouch.

To investigate the mechanism of ICW formation, we systematically inhibited Ca^{2+} signaling genes using RNAi when stimulated with 15% v/v FEX. Importantly, we found significantly fewer ICWs when *Plc21C*, *IP_3R*, or *Gαq* were knocked down (Fig. 4, *A–D*; Videos S11, S12, and S13). Knockdown of *Plc21C* still resulted in localized cell-level spike activity but not ICWs. This suggests PLC is either

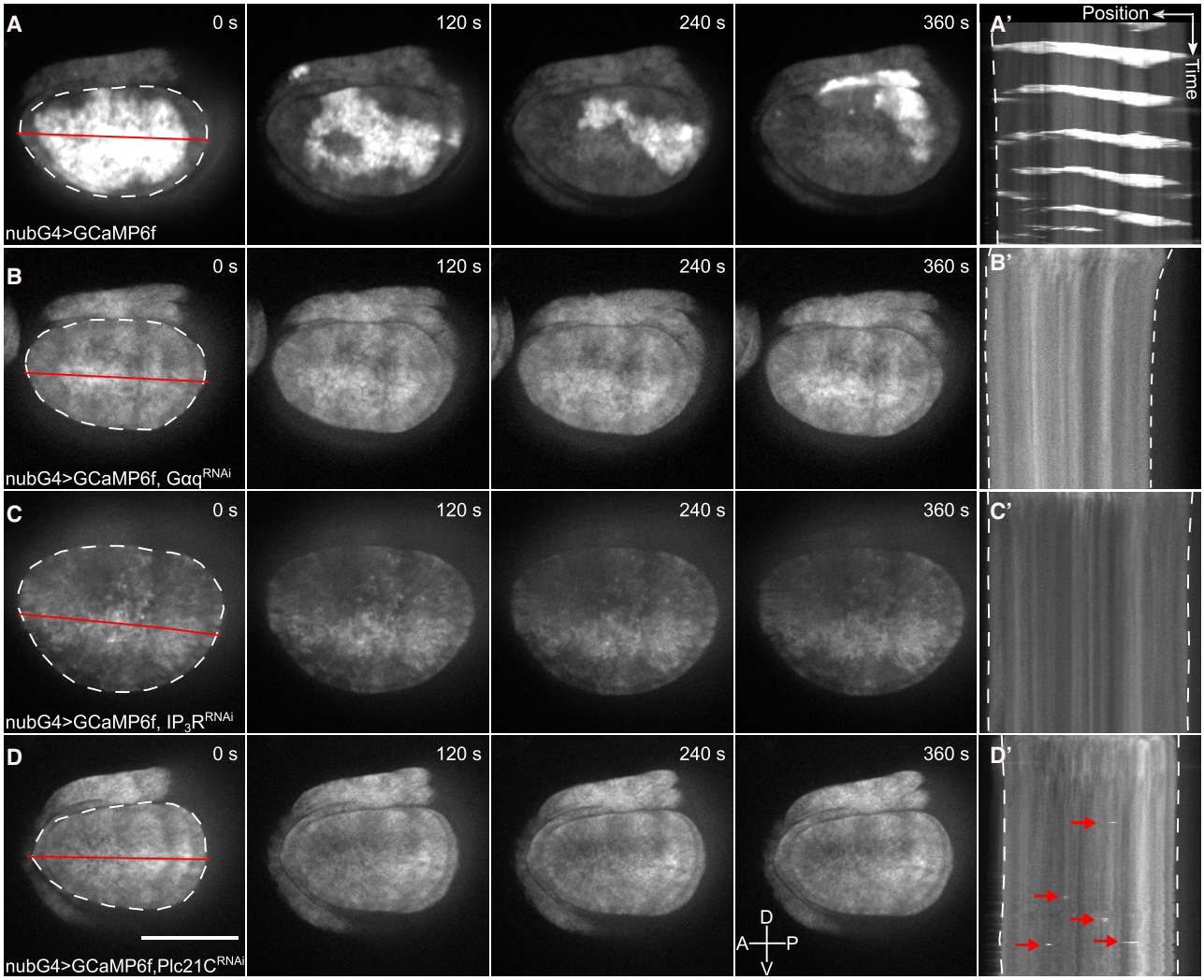

FIGURE 4 FEX-induced calcium waves require GPCR/Gαq signaling. (*A–D*) Montages from ex vivo time-lapse videos and (*A′–D′*) kymographs of the corresponding time-lapse videos are shown. The genotypes of the wing discs are indicated on the bottom left. We observed ICWs in (*A*) and no Ca^{2+} signaling activity in (*B–D*). The cross indicates the orientation of the wing disc (Videos S10, S11, S12, and S13). The red arrows indicate single-cell spikes. Position and timescale bars, 25 μm and 15 min. White dotted line represents the pouch boundary. Red line represents the *x-y* position of the kymograph. The RNAi lines are as follows: $G\alpha q^{RNAi}$, BL#36775; IP_3R^{RNAi}, BL#25937; and $Plc21C^{RNAi}$, BL#31719. To see this figure in color, go online.

partially knocked down, or there is redundancy between PLC isoforms (Fig. 4 *D*). Overall, these results demonstrate that FEX-induced ICWs require GPCR/Gαq-based signaling. Thus, our ex vivo results provide additional insights into the mechanism of intercellular Ca^{2+} signaling propagation in the wing disc.

Calcium signaling dynamics are regulated during wing disc development

In vivo Ca^{2+} transients were noted in previous reports. However, a systematic characterization has not been performed because of the technical challenges of in vivo imaging. To address this knowledge gap, we tested whether in vivo Ca^{2+} signaling activity is a regulated phenomenon. We gently immobilized the larvae with tape on a coverslip to enable in vivo imaging for durations of 20 min. We developed a semi-automated pipeline to blindly classify Ca^{2+} signaling activity in video segments, matching the qualitative ex vivo analysis. Interestingly, we identified and quantified the same four classes of Ca^{2+} signaling activity that are observed ex vivo (Fig. 3, *E* and *E′*): 1) local Ca^{2+} spikes (Fig. 5 *A*; Video S1), 2) ICTs (Fig. 5 *B*; Video S2), 3) ICWs (Fig. 5 *C*; Video S3), and 4) fluttering (Fig. 5 *D*; Video S4).

Next, we quantified the percentage of four classes in wing discs of different ages and sizes throughout development (n = 103 videos). We found that observable Ca^{2+} signaling activity decreases from 27% to 6% of the time from 5 to 8 days AEL (Fig. 5 *E*). Ca^{2+} signaling activity also shifts from fluttering and ICW classes at day 5 to spikes and

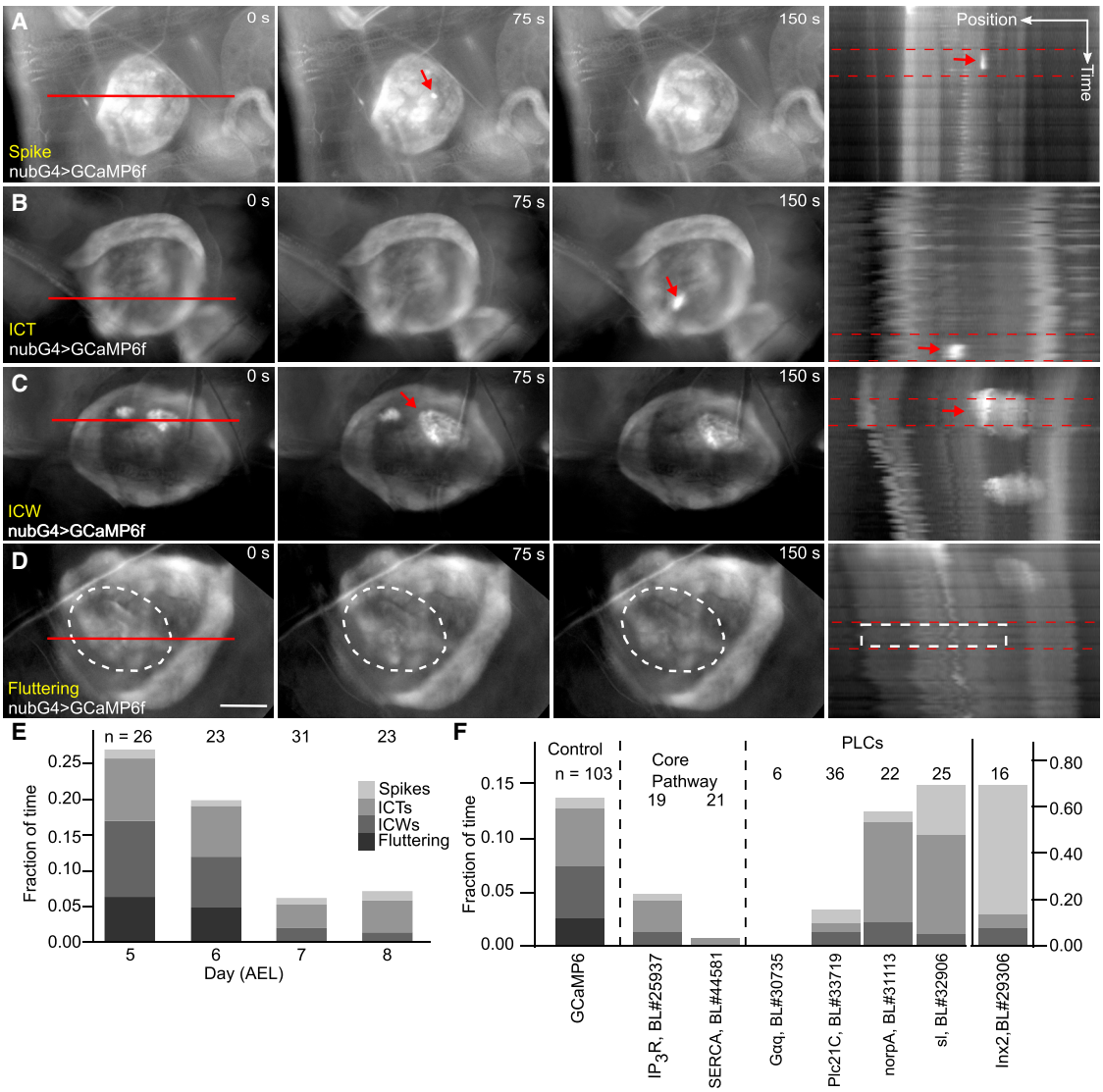

FIGURE 5 Overall calcium activity decreases throughout development in vivo and is regulated by multiple PLCs. (*A–D*) Montages from in vivo time-lapse videos of *nub > GCaMP6f* larval wing discs are shown. A diverse range of Ca^{2+} dynamics are observed. The red lines represent the *x-y* position of the kymograph and are 200 μm long. The red arrows indicate the Ca^{2+} events. The white circle indicates the area of fluttering Ca^{2+} oscillation. Because of its nature, the supporting videos demonstrate the fluttering oscillation much more clearly (Videos S1, S2, S3, and S4). (*A′–D′*) The kymograph of the corresponding time-lapse videos is shown. The kymographs between red dotted lines correspond to the montage on the left. Scale bars, 50 μm. Position and timescale bars, 50 μm and 5 min. (*E*) The duration of each category of Ca^{2+} oscillation as a fraction of total time is shown. The total Ca^{2+} activation time (the height of the column) decreases as wing disks grow older. $p < 10^{-15}$ by ordinal regression. (*F*) In vivo Ca^{2+} signaling transients are regulated by multiple PLC isoforms, either through Gαq/PLCβ (Plc21C), which greatly inhibits large waves, or RTK/PLCγ, which also modulates Ca^{2+} signaling levels. Videos S5, S6, S7, S8, S9, and S10 provide representative examples for each genetic perturbation. For Inx2, the *y*-axis is on the right, showing upregulation of small cellular spikes. Labels represent crosses of UAS-RNAi lines to parental *nub* > GCaMP6f line. AEL indicates days after egg laying. To see this figure in color, go online.

ICTs at day 8 (Fig. 5 *E*, $p < 10^{-15}$ by ordinal regression). Note, the GCaMP6f test line shows slower growth compared to nontransgenic flies, resulting in delayed larval development.

To verify the mechanisms regulating in vivo Ca^{2+} activity, we performed similar perturbations with *UAS-RNAi* lines (Fig. 5 *F*; Tables S6 and S7; Videos S5, S6, S7, S8, S9, and S10). We observed that genetically knocking down *SERCA* and *IP$_3$R* greatly reduced Ca^{2+} signaling activity. Perturbation of GPCR-stimulated signaling through $Plc21C^{RNAi}$ inhibited ICWs. Perturbation of RTK signaling through *sl/PLCγ* also reduced the observed proportion of higher classes of Ca^{2+} signaling activity but increased the proportion of time with observed cellular spikes (Fig. 5 *F*; Tables S6 and S7). The disruption of gap junctions through $Inx2^{RNAi}$ led to a significant increase in the number of spikes throughout the tissue, but Ca^{2+} signals did not travel from cell to cell across the tissue. This suggests that gap-junction

communication synchronizes Ca^{2+} activity across the tissue and leads to the reduced frequency of initial stimulatory events. The increase in cellular Ca^{2+} spike activity with gap junctions inhibited may suggest that it is easier to stimulate smaller systems. $Inx2^{RNAi}$-expressing wings are significantly smaller, suggesting the possibility that part of the growth phenotype is due to reduced coordination in Ca^{2+} signaling synchronization between cells.

To summarize, the multiple classes of observed Ca^{2+} signaling activity are a recurring phenomenon during in vivo development (29). Importantly, we found that Ca^{2+} signaling activity in wing discs correlate with the larval age. This correlation suggests that Ca^{2+} signaling activity decreases as wing discs approach their final size (Fig. 5 *E*).

Calcium signaling activity is spatiotemporally patterned by morphogen signaling

It is challenging to perform quantitative spatial analysis of Ca^{2+} signaling in vivo because of larval motion, optical interference from the cuticle, and limited imaging duration. To overcome this challenge, we developed a quantitative pipeline to analyze ex vivo-imaged wing discs, which enabled more detailed spatiotemporal analysis (Fig. 6; Fig. S1–S4). In these experiments, we stimulated Ca^{2+} signaling with 15% FEX and recorded and analyzed Ca^{2+} signaling responses under a range of genetic perturbations. We then inferred how the "organ state" influences the calcium responses.

As suspended micro-organs, wing discs often exhibit movement, even in ex vivo cultures. Image registration is a problem with dynamic systems because the most distinct landmarks in the image are constantly changing as the signal moves along the tissue. To solve this problem, we built a pipeline that detects the borders of the pouch using a deep neural network approach that transforms the underlying images onto the initial mask (Figs. 6, *A* and *B* and S4; (46)). Ca^{2+} signatures were extracted from signals that are taken from a square grid across the tissue (Fig. 6, *C* and *D*). The resulting spatial maps were transformed onto a canonical domain represented by the average positions of the pouch boundaries and axes using a previously described method (Fig. 6 *E*; (55)). Finally, we report the median of the spatial maps (Fig. 6 *F*).

The spatial analysis revealed that a time-averaged patterning of amplitude emerges as the wing disc grows bigger. Across all wing discs, the average amplitude is 33% higher in the posterior compartment than in the anterior compartment (Fig. 7 *A*). In smaller discs (area $< 1.6 \times 10^4$ μm^2), the difference of amplitude between the anterior compartment and the posterior compartment is not significant (Fig. 7 *B*). In larger discs (area $> 1.6 \times 10^4$ μm^2), the patterning of amplitude emerges between the anterior and the posterior compartments, in which the amplitude is lower in the anterior compartment and higher in the posterior compartment, and the difference is significant (Fig. 7 *B*).

The discovery of anterior-posterior patterning of amplitudes suggests that upstream morphogen pathways may

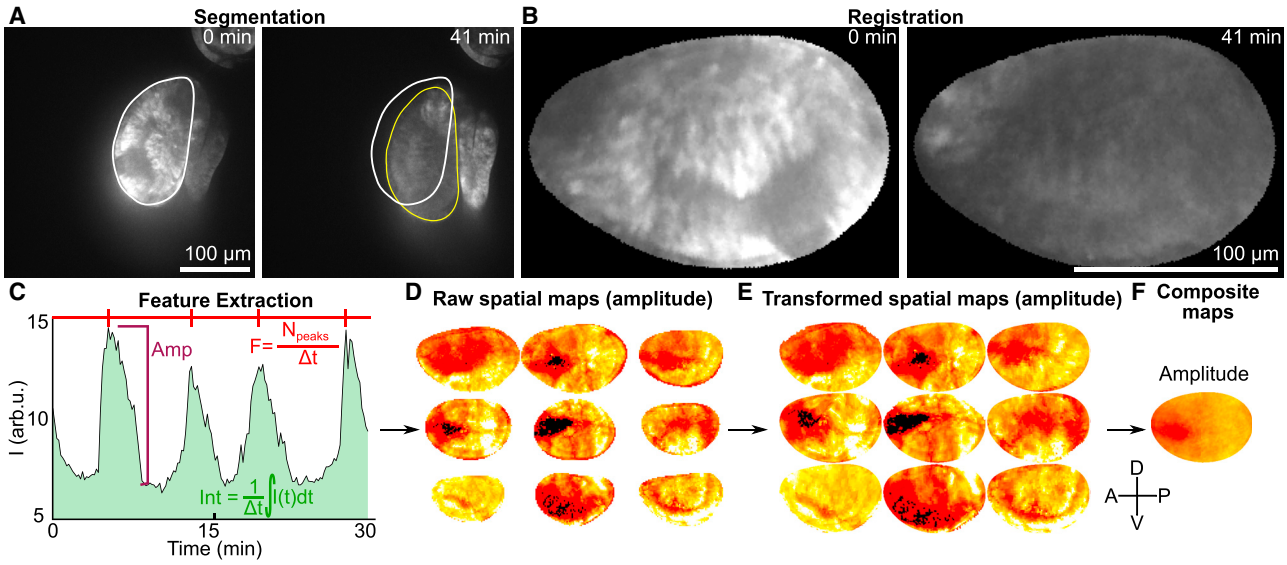

FIGURE 6 Pipeline for spatiotemporal quantification of calcium signatures. (*A*) Automatic segmentation of pouch region with deep-learning segmentation algorithm was developed for this study. Outlines represent the pouch at the initial time point (*white*) and the final time point (*yellow*). (*B*) Registration of raw images onto canonical pouch shapes is shown. (*C*) Extraction of amplitudes (Amp), frequency (F), and integrated intensity (Int) from Ca^{2+} traces for individual region of interest (ROI) was performed. (*D*) The Ca^{2+} signature is computed for each spatial position within each pouch to generate a spatial map. (*E*) Each spatial map is transformed onto a canonical coordinate system to align the anterior-posterior and dorsal-ventral axes. (*F*) Each set of transformed spatial maps is averaged at each position to generate a composite spatial map. The cross indicates the orientation of the wing disc. Scale bars, 100 μm. To see this figure in color, go online.

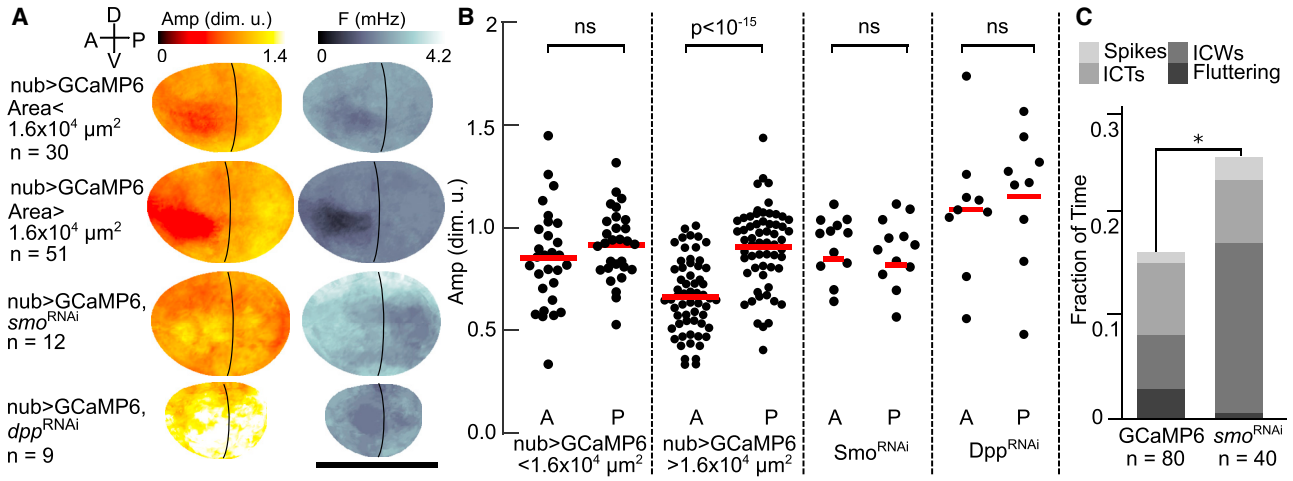

FIGURE 7 Calcium signaling is spatially patterned in the developing wing disc. (*A*) Composite spatial maps of median summary statistics of Ca^{2+} features are shown. Wing disc pouches expressing *nub > GCaMP6f* were grouped by pouch size. These wing disc pouches followed one of two patterns: small pouches ($<1.6 \times 10^4$ μm^2) with uniformly high amplitude in both compartments and larger pouches ($>1.6 \times 10^4$ μm^2) with a lower median amplitude in the anterior compartment. Inhibition of Hh and Dpp signaling led to an increase in frequency (F) and uniformly high amplitude. The black curve represents the approximate anterior-posterior boundary. Orientations of the wing discs are indicated in upper left corner. (*B*) The amplitude measurement of anterior and posterior compartments in control discs (*small* and *large*) and smo^{RNAi} and dpp^{RNAi} discs are shown. In *nub > GCaMP6f* discs, the difference of amplitude between the two compartments is significant in large disks. The difference is not significant in smo^{RNAi} (composite of three independent RNAi lines, Fig. S9) and dpp^{RNAi} discs, and the median amplitude appears uniform near the anterior dorsal-ventral boundary region. The *p* values were obtained by paired *t*-tests. (*C*) Inhibition of Hh signaling by smo^{RNAi} increases overall Ca^{2+} signaling activity in wing discs in vivo. Sample size represents the number of analyzed videos. Scale bars, 200 μm. Total Ca^{2+} activity by proportions test as described in Tables S6 and S7. To see this figure in color, go online.

affect Ca^{2+} dynamics. To test this, we perturbed the Hh signaling pathways, which direct the development of the anterior-posterior compartment boundary (56). Smoothened (Smo), a GPCR (57), is a primary transducer of Hh signaling (58). We also perturbed Dpp signaling, which is downstream of Hh signaling and also directs anterior-posterior patterning and growth (35,39,59). We knocked down *smo* and *dpp* using RNAi expression in the wing disc pouches of wandering larvae to test if the spatial asymmetry in average amplitudes is downstream of Hh signaling (*nub > GCaMP6f > smo*^{RNAi}; Video S21) or Dpp signaling (*nub > GCaMP6f > dpp*^{RNAi}; Video S22). We found that inhibition of either Hh or Dpp signaling was sufficient to abolish anterior-posterior spatial patterning of ICW amplitudes and leads to a higher frequency in the entire pouch (Fig. 7, *A* and *B*). These results were confirmed by evaluating multiple independent RNAi lines against *smo*, which are reported individually in Fig. S9, and combined together in Fig. 7, *A* and *B*. Further, the results of increased activity of *nub > GCaMP6f > smo*^{RNAi} were replicated in vivo (Fig. 7 *C*). Hh suppression resulted in roughly doubling the amount of time when fluttering or ICWs were observed in the pouch (Fig. 7 *C*). Additionally, Hh suppression led to a decrease in the average pouch size for wandering larvae, which are near the end of development. These results demonstrate that spatial patterning of the amplitude of Ca^{2+} oscillations is downstream of Hh and Dpp signaling, which are two morphogen pathways involved in regulating patterning and tissue growth. It provides support for a model in which agonist-stimulated Ca^{2+} signaling activity provides a readout of morphogenetic states of the organ during development.

Calcium signaling activity decreases with wing disc pouch size in a power-law relationship

To determine how stimulated Ca^{2+} signaling dynamics change as wing disc sizes increase, we created a high-dimensional summary map relating organ size to the features of Ca^{2+} signaling (Fig. 8 *A*; Videos S20, S21, S22, S23, and S24). We plotted the integrated intensity and frequency of Ca^{2+} signaling activity of all wing disc imaged against their pouch sizes (with wing disc pouch size as a proxy for overall organ size). The result demonstrates several interesting correlations between features of Ca^{2+} signaling activity and wing disc sizes, which form a manifold in high-dimensional morphological-cell signaling space (Fig. 8, *A–C*). Integrated intensity was found to decrease with pouch size (Fig. 8 *B*). Additionally, we found that frequency increases with integrated intensity and then decreases again (Fig. 8 *C*). Further, we analyzed the full data set for qualitative characteristics of calcium signaling, similar to the in vivo experiments. We found that there is a progression from fluttering disc to oscillatory waves to smaller-scale stochastic spiking activity (Fig. 8 *B*). Overall, these findings further confirm stimulated Ca^{2+} signaling responses decline with increasing organ size until the end of larval development.

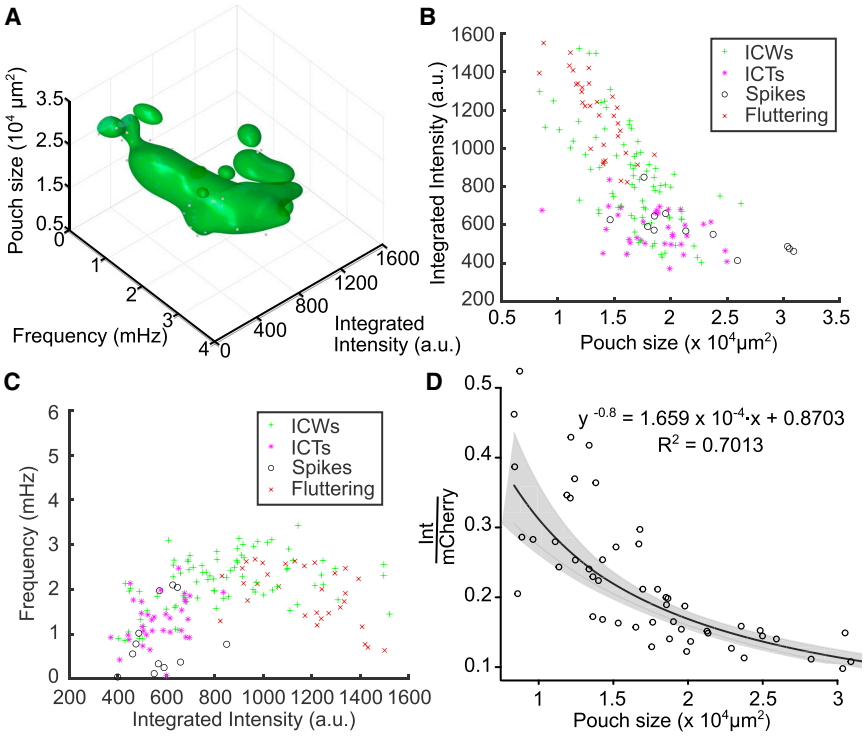

FIGURE 8 Transitions of agonist-stimulated calcium signaling as a function of pouch size. (*A*) Larval wing discs exhibit transitions in FEX (Gαq) agonist-stimulated Ca^{2+} signaling dynamics during development, forming a spiral in a three-dimensional plot of "morphological cell signaling space." (*B*) Integrated intensity decreases with increasing pouch size. Colors represent dominant Ca^{2+} dynamics observed in the particular sample. (*C*) A parametric plot of a data set from (*A*) shows frequencies of Ca^{2+} oscillations increasing with increasing integrated intensity and then decreasing at higher amplitudes. Note that low-amplitude fluttering does not contribute to the measured frequency signal. Each wing disc was imaged for 1 h and with a 10 s interval. Each video was divided into 31 time segments. As a second level of analysis, dominant Ca^{2+} activity was scored blindly in each segment, respectively (*colors*, see legend). Ca^{2+} dynamics that were observed for the largest total time for each separate wing disc sample are represented as color dots in (*B* and *C*). (*D*) A regression curve fit to ratiometric average integrated intensity of Ca^{2+} signaling in wing pouches as a function of pouch size is shown (n = 53). To see this figure in color, go online.

The full data set plotted in Fig. 8, *A–C* includes a subset of discs that also expressed a red fluorescent protein under the same Gal4 driver (expressing *nub > GCaMP6f/ > mCherry*; Video S24). Similar results between *nub > GCaMP6f* and *nub > GCaMP6f/ >mCherry* suggest Gal4 dilution is not a significant concern (Fig. S6 *E*). For discs coexpressing mCherry, we could normalize GCaMP6f fluorescence to mCherry fluorescence (Fig. S6 *C*). This allowed us to obtain ratiometric estimates of Ca^{2+} signaling that better account for sensor expression. For the data with mCherry expression, we observed a power-scaling relationship in which average ratiometric integrated intensity (normalized to mCherry expression) scales with pouch area ($R^2 = 0.70$, Fig. 8 *D*; Figs. S7 and S8). This relationship utilizes a Box-Cox power-scaling transformation (60) to maximize the log-likelihood estimation of the power exponent (Fig. S6 *A*). This power-scaling relationship served as a better fit compared to linear and exponential models because of a more normal distribution of residuals and the least variance between model residual values (Fig. S7).

Calcium signaling responds to perturbations to morphogen and growth factor signaling

Finally, we investigated the effects of multiple regulators of organ growth to further clarify the connections between organ growth and stimulated Ca^{2+} responses. We ectopically activated the Dpp pathway through the uniform expression of the constitutively active form of the Dpp receptor, tkv^{CA} (39,61,62). Additionally, we ectopically stimulated growth through the inhibition of the tumor suppressor phosphatase and tensin homolog (*Pten*), which results in high levels of insulin/AKT signaling without impacting wing patterning (63,64; Video S23). According to previous reports, both conditions lead to increases in cell division and growth (35,59,65). We found that these growth-inducing perturbations resulted in a decrease in Ca^{2+} signaling activity relative to control discs when exogenously stimulated (Fig. 9, *A* and *B*, *orange*). Inhibiting Hh and Dpp signaling with smo^{RNAi} and dpp^{RNAi} expression, respectively, lead to reduced growth (Fig. S8) and shows an increased integrated intensity, amplitude, and frequency of Ca^{2+} oscillations in wing disc pouches (Fig. 9, *A* and *B*, *blue solid points* of various shapes).

In sum, our results provide multiple lines of evidence that reveal general trends when wing disc growth is perturbed: morphogenetic perturbations that reduce growth lead to abnormally higher levels of integrated Ca^{2+} signaling activity above the manifold, relating size to integrated Ca^{2+} activity. In contrast, perturbations that promote growth lead to reduced levels of total (integrated) Ca^{2+} signaling.

DISCUSSION

Here, we have performed a systems-level analysis of Ca^{2+} signaling in a model system of organ growth and morphogenesis. To do so, we have established an innovative "Ca^{2+} decoding" image-processing pipeline. This work

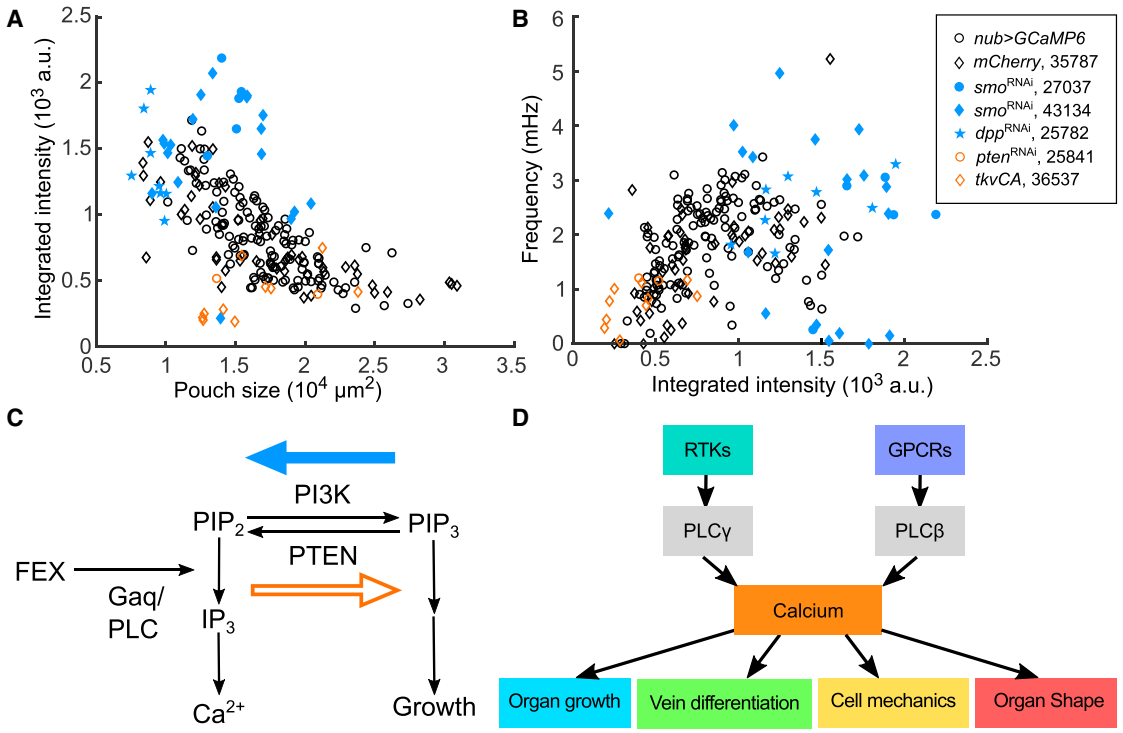

FIGURE 9 Integrated model of calcium signaling transduction in the *Drosophila* wing disc. (*A*) Genetic perturbations impacting morphogen and growth pathways result in deviations in agonist (FEX)-stimulated Ca^{2+} signaling responses. Data points of different colors and shapes represent wing discs with various genotypes that are indicated in the legend. Blue-colored, solid data points result in patterning defects and reduced wing growth. Higher Ca^{2+} signaling responses are produced for a given stimulus (15% FEX in all cases). Orange-colored, nonsolid data points result in increased growth. Reduced Ca^{2+} signaling responses are observed for the same stimulus. (*B*) The parametric plot of the same data set shows increased frequency in Ca^{2+} transients for the growth-suppression perturbations and a decreased frequency for growth-enhancement perturbations. Bloomington stock numbers for UAS-RNAi transgenic lines are included. All the perturbations shown here were driven by the *nub > GCaMP6f* tester line. (*C*) An inferred model is shown consistent with observations in (*A*) and (*B*). (*D*) Schematic summarizing key findings from this work and the literature is shown. Both RTK/PLC$\gamma-$ and GPCR/PLCβ-based signaling contributes to Ca^{2+} activity in vivo and ex vivo (inputs). Perturbations to core Ca^{2+} signaling pathway result in a range of developmental phenotypes (outputs), including wing size, vein differentiation, cell mechanics, and overall tissue shape. To see this figure in color, go online.

advances the analysis of Ca^{2+} signaling dynamics in organ systems. It demonstrates how a significant portion of cellular information processing occurs through the coupling of signaling dynamics during organ development. This pipeline also can be used to develop spatiotemporal maps of larval wing growth and patterning for other signal integrators such as cAMP (66) and for readouts of central growth pathways such as Hippo signaling (67).

This work has established multiple inputs and outputs for the calcium bow-tie network during wing development (Fig. 9 *D*). We also identified four classes of spontaneous Ca^{2+} signaling activity during in vivo development in the wing disc: 1) cellular Ca^{2+} spikes, 2) ICTs, 3) ICWs, and 4) elevated Ca^{2+} fluttering. We found that increasing Gαq-mediated signaling with increasing concentrations of FEX leads to a natural progression from low (class 1 and 2) to higher levels of Ca^{2+} signaling responses (classes 3 and 4). These four signaling classes occur both ex vivo and in vivo. Importantly, we found that multiple classes of Ca^{2+} activity occur and are a regulated phenomenon in vivo. These findings contradict previous suggestions that ICWs may be an ex vivo artifact (26,68). Future work is needed to specify the full set of specific RTKs, GPCRs, and morphogens that modulate Ca^{2+} dynamics in vivo.

We demonstrated a negative correlation between the stimulated Ca^{2+} signaling responses and the wing disc age and size for third instar larvae. Overall, these observations provide evidence for Ca^{2+} signaling as a readout for overall organ size in the developing wing and a regulator of cellular processes during larval wing development. Through linear regression analysis, we demonstrated a negative power-law correlation between larval age/pouch size and integrated Ca^{2+} signaling activity. These findings suggest that Ca^{2+} signaling decreases during the latter stages of larval wing disc growth. The maximal log-likelihood estimation of the power exponent occurred when the estimate had a value of -0.8 ± 0.5. This is consistent with many allometric scaling relationships observed in biological systems wherein quarter-power scaling frequently occurs (69,70). For example, quarter-power scaling has been observed in the organism metabolic rate, lifespan, growth rate, heart rate, and the concentrations of metabolic enzymes (69).

A −0.75-scaling relationship is consistent, near the maximal log-likelihood estimation, and within the 95% confidence interval of the optimal exponent power (Fig. S6 *A*). This, in turn, may indicate that the underlying metabolic trajectory of organ growth influences the level of agonist-stimulated calcium signaling activity.

Further, we observed anterior-posterior patterning of Ca^{2+} signaling activity amplitudes in the wing disc. The amplitude is higher in the posterior than in the anterior compartment. As these compartments have been shown to grow at different rates, this result is consistent with the correlation between Ca^{2+} signaling activity and the growth state of each compartment (71). There are several possible explanations for why there is an absence of amplitude patterning between anterior and posterior compartments for larger discs in Hh (smo^{RNAi}) or Dpp (dpp^{RNAi}) signaling-perturbed discs. First, Hh and Dpp signaling may be directly responsible for patterning the anterior-posterior amplitude difference, perhaps through regulation of cAMP levels (72,73). Second, this may be because the sizes of anterior and posterior compartments are similar under those conditions. Identifying the cause of this phenomenon may yield insight into additional patterning roles for Ca^{2+} signaling in wing development, including the pupal stages when vein differentiation occurs. Recently, Ca^{2+} signaling has been connected to proper Hh signaling in zebrafish embryo (74). Our work suggests that Ca^{2+} signaling may generally be involved in modulating morphogenesis mediated by Hh signaling and other morphogen pathways.

Future work is needed to identify specific mechanisms connecting signal transduction inputs to phenotypic outputs. In a recent article, cellular Ca^{2+} spikes were found to correlate with secretion of Dpp, a key regulator of wing disc size and tissue patterning (23). We speculate that local cellular spike activity might be connected to the positive regulation of organ growth. Smo^{RNAi} and dpp^{RNAi} leads to smaller wing discs and higher integrated Ca^{2+} intensity when Ca^{2+} signaling is stimulated by agonists. The data points from growth-reducing perturbation (smo^{RNAi} and dpp^{RNAi}, *blue solid data points*) lie above the negative correlation curve of the control wing discs (*black circle* or *diamond data points*, Fig. 9, *A* and *B*). In contrast, genetic perturbations leading to more growth (tkv^{CA} and $Pten^{RNAi}$, *orange data points*, Fig. 9, *A* and *B*) result in reduced Ca^{2+} signaling responses when stimulated.

These results imply a common underlying regulatory mechanism. As a launching point for future work, we speculate by proposing a simple model that explains the results reported here (Fig. 9 *C*). First, our experiments demonstrate that FEX stimulates $G\alpha q/PLC\beta$ activity, which results in IP_3 generation and IP_3-regulated Ca^{2+} release. Sufficient IP_3 production may lead to phosphatidylinositol bisphosphate (PIP_2) substrate depletion. In other systems, PIP_2 is often rate limiting for Ca^{2+} signaling (75,76). PIP_2 is also required for phosphatidylinositol trisphosphate generation, which then stimulates cell growth through PI_3K/AKT signaling (77). It follows that reduced PI_3K signaling resulting from decreased growth stimulation (indirectly through inhibition of Hh or Dpp signaling in our experiments) will lead to higher PIP_2 substrate availability and a stronger Ca^{2+} response. Conversely, decreased PIP_2 availability through the inhibition of PTEN (which converts phosphatidylinositol trisphosphate to PIP_2) (63,65) or through constitutively active Dpp signaling (78) would lead to attenuated Ca^{2+} signaling responses when stimulated by FEX (Fig. 9 *C*).

This interpretation of the data provides a generalizable and testable hypothesis for future work: if PIP_2 levels are more abundant (reduced PI_3K signaling and growth activity), more IP_3 can be generated, resulting in more Ca^{2+} signaling for a given agonist response. If PIP_2 substrate levels are limiting (as results when PTEN is inhibited or more growth is stimulated), less IP_3-stimulated Ca^{2+} signaling can occur. This hypothetical model would predict that sufficient overexpression of $G\alpha q$ could lead to reduced organ growth by depleting PIP_2 substrate availability for growth stimulation. Future work may identify such relationships across biological systems because all of these molecular components are present in most eukaryotic cells. We term this hypothetical model the "Ca^{2+} shunt" hypothesis of growth control.

Ca^{2+} signaling likely modulates other aspects of growth control during larval development. Ca^{2+} may integrate signals about the availability of nutrients or about mechanical constraints on the tissue. Several known effectors of size control pathways, such as *kibra*, a regulator of Hippo signaling (79–81), have Ca^{2+} signaling binding domains as annotated by InterPro (82).

Additionally, this work motivates new questions regarding how gap-junction communication, and by extension, membrane voltage, influences the overall control of organ size (4). A decrease in cell-cell gap-junction permeability occurs over the course of wing development (83). As gap junctions become less permeable, Ca^{2+} and IP_3 diffuse a shorter distance before being reabsorbed into the endoplasmic reticulum or decaying, respectively. This would explain the transition from ICWs to ICTs and spikes as well as why amplitude is spatially patterned in large discs as development proceeds. Other studies have also implicated gap-junction communication in organ size control (84). For example, $Inx2^{RNAi}$ suppresses growth in the developing eye disc (85). *Connexin43* mutants that disrupt gap-junction communication lead to short fin in zebrafish (86). Gap-junction communication also regulates cell differentiation as Inx2-mediated Ca^{2+} flux is essential for border cell specification in *Drosophila* (87). Our results suggest that part of the role of gap-junction communication in regulating size and influencing tissue patterning is through the regulation of Ca^{2+} transients across the tissue. Taken together, it is

therefore likely that the role of Ca^{2+} signaling in wing growth is conserved in other organs.

Our phenotypic analysis provides additional evidence that the Ca^{2+} signaling module contributes to modulating wing morphogenesis during pupal development and vein cell differentiation. It should be noted that the crossvein defects suggest that these veins are particularly sensitive to levels of morphogen signaling, including Dpp (88). In particular, Dpp signaling has been linked to Ca^{2+} signaling in the developing wing (23). Perturbing Ca^{2+} signaling may also be enhancing the crossvein defects that can occur in the MS1096-Gal4 line, which impacts *Beadex* gene function (89). Future work will need to investigate the mechanisms leading to wing shape and vein differentiation defects, which are specified during pupal development.

Computational modeling is essential for future efforts to decode the regulation and function of Ca^{2+} signaling (3). Understanding the specific roles of Ca^{2+} signaling in organ development will require computational models that couple multiple signals of Ca^{2+} signaling across multiple spatio-temporal scales (90–93). For example, computational models are particularly useful at the systems level to understand mechanisms for the coupled transport of Ca^{2+} and wound healing (6). Regarding this study, our findings that the integrated Ca^{2+} intensity decreases with development is consistent with a model from the neocortex being applied to our wing disc, in which Ca^{2+} signaling dynamics are weakly coupled with cell-cycle progression and can influence cell-cycle synchrony with neighbors (94,95). In sum, this effort demonstrates key roles of Ca^{2+} signaling as a signal integrator in epithelial growth and morphogenesis.

SUPPORTING MATERIAL

Supporting Materials and Methods, 11 figures, 7 tables, and 24 videos are available at http://www.biophysj.org/biophysj/supplemental/S0006-3495(19)30023-2.

AUTHOR CONTRIBUTIONS

J.J.Z., Q.W., P.A.B., and C.N. designed and conceived the study. Q.W., D.K.S., F.J.H., C.N., M.K.L, and N.A.-W. performed experiments. P.A.B. developed methods for feature extraction, statistical analysis, and manual annotation. P.A.B. and F.J.H. implemented qualitative analysis pipeline, performed statistical analysis, and performed manual classification of in vivo data. J.C., P.L., and D.Z.C. developed automated methods for image segmentation and registration. Q.W., P.A.B., F.J.H., and J.J.Z. analyzed data and wrote the manuscript. J.J.Z supervised the study.

ACKNOWLEDGMENTS

We thank Mark Alber, Christopher Paolucci, Jeffrey Kantor, Gregory Reeves, Alyssa Lesko, Erin Howe, and Yogesh Goyal for helpful feedback, Brandon Greenawalt (Notre Dame Center for Social Research) for helpful conversations regarding statistical methodology, Simon Restrepo for sharing early unpublished observations, Jahmel Jordon and Kara Snyder for technical support, and members of the Zartman Lab for critiques.

The work in this manuscript was supported in part by National Institutes of Health grant R35GM124935, National Science Foundation awards CBET-1403887, CBET-1553826, CNS-1629914, CCF-1217906, and CCF-1617735, Harper Cancer Research Institute Research like a Champion awards (Q.W.), Walther Cancer Foundation Interdisciplinary Interface Training Project (P.A.B.), and the Notre Dame Advanced Diagnostics & Therapeutics Berry Fellowship (C.N.). The authors gratefully acknowledge the Notre Dame Integrated Imaging Facility.

REFERENCES

1. Dodd, A. N., J. Kudla, and D. Sanders. 2010. The language of calcium signaling. *Annu. Rev. Plant Biol.* 61:593–620.
2. Csete, M., and J. Doyle. 2004. Bow ties, metabolism and disease. *Trends Biotechnol.* 22:446–450.
3. Brodskiy, P. A., and J. J. Zartman. 2018. Calcium as a signal integrator in developing epithelial tissues. *Phys. Biol.* 15:051001.
4. Levin, M., and C. J. Martyniuk. 2018. The bioelectric code: an ancient computational medium for dynamic control of growth and form. *Biosystems.* 164:76–93.
5. Berridge, M. J., P. Lipp, and M. D. Bootman. 2000. The versatility and universality of calcium signalling. *Nat. Rev. Mol. Cell Biol.* 1:11–21.
6. Antunes, M., T. Pereira, …, A. Jacinto. 2013. Coordinated waves of actomyosin flow and apical cell constriction immediately after wounding. *J. Cell Biol.* 202:365–379.
7. Deng, H., A. A. Gerencser, and H. Jasper. 2015. Signal integration by Ca^{2+} regulates intestinal stem-cell activity. *Nature.* 528:212–217.
8. Hayashi, K., T. S. Yamamoto, and N. Ueno. 2018. Intracellular calcium signal at the leading edge regulates mesodermal sheet migration during Xenopus gastrulation. *Sci. Rep.* 8:2433.
9. Lam, P. Y., S. E. Webb, …, A. L. Miller. 2009. Inhibition of stored Ca^{2+} release disrupts convergence-related cell movements in the lateral intermediate mesoderm resulting in abnormal positioning and morphology of the pronephric anlagen in intact zebrafish embryos. *Dev. Growth Differ.* 51:429–442.
10. Markova, O., and P. F. Lenne. 2012. Calcium signaling in developing embryos: focus on the regulation of cell shape changes and collective movements. *Semin. Cell Dev. Biol.* 23:298–307.
11. Markova, O., S. Sénatore, …, P. F. Lenne. 2015. Calcium spikes in epithelium: study on *Drosophila* early embryos. *Sci. Rep.* 5:11379.
12. Monteith, G. R., D. McAndrew, …, S. J. Roberts-Thomson. 2007. Calcium and cancer: targeting Ca^{2+} transport. *Nat. Rev. Cancer.* 7:519–530.
13. Noren, D. P., W. H. Chou, …, A. Levchenko. 2016. Endothelial cells decode VEGF-mediated Ca^{2+} signaling patterns to produce distinct functional responses. *Sci. Signal.* 9:ra20.
14. Prevarskaya, N., R. Skryma, and Y. Shuba. 2011. Calcium in tumour metastasis: new roles for known actors. *Nat. Rev. Cancer.* 11:609–618.
15. Restrepo, S., and K. Basler. 2016. Drosophila wing imaginal discs respond to mechanical injury via slow $InsP_3R$-mediated intercellular calcium waves. *Nat. Commun.* 7:12450.
16. Wallingford, J. B., A. J. Ewald, …, S. E. Fraser. 2001. Calcium signaling during convergent extension in Xenopus. *Curr. Biol.* 11: 652–661.
17. Berridge, M. J. 1997. The AM and FM of calcium signalling. *Nature.* 386:759–760.
18. Ohno, Y., and J. M. Otaki. 2015. Spontaneous long-range calcium waves in developing butterfly wings. *BMC Dev. Biol.* 15:17.
19. York-Andersen, A. H., R. M. Parton, …, T. T. Weil. 2015. A single and rapid calcium wave at egg activation in Drosophila. *Biol. Open.* 4:553–560.
20. Chernoff, E. A., and S. R. Hilfer. 1982. Calcium dependence and contraction in somite formation. *Tissue Cell.* 14:435–449.

21. Kaneuchi, T., C. V. Sartain, …, M. F. Wolfner. 2015. Calcium waves occur as Drosophila oocytes activate. *Proc. Natl. Acad. Sci. USA.* 112:791–796.

22. Belgacem, Y. H., and L. N. Borodinsky. 2011. Sonic hedgehog signaling is decoded by calcium spike activity in the developing spinal cord. *Proc. Natl. Acad. Sci. USA.* 108:4482–4487.

23. Dahal, G. R., S. J. Pradhan, and E. A. Bates. 2017. Inwardly rectifying potassium channels influence *Drosophila* wing morphogenesis by regulating Dpp release. *Development.* 144:2771–2783.

24. Hříbková, H., M. Grabiec, …, Y. M. Sun. 2018. Calcium signaling mediates five types of cell morphological changes to form neural rosettes. *J. Cell Sci.* 131:jcs206896.

25. Takano, K., S. Obata, …, M. Asashima. 2011. Development of Ca^{2+} signaling mechanisms and cell motility in presumptive ectodermal cells during amphibian gastrulation. *Dev. Growth Differ.* 53:37–47.

26. Balaji, R., C. Bielmeier, …, A. K. Classen. 2017. Calcium spikes, waves and oscillations in a large, patterned epithelial tissue. *Sci. Rep.* 7:42786.

27. Narciso, C., Q. Wu, …, J. Zartman. 2015. Patterning of wound-induced intercellular $Ca(^{2+})$ flashes in a developing epithelium. *Phys. Biol.* 12:056005.

28. Wu, Q., P. A. Brodskiy, …, J. J. Zartman. 2017. In vivo relevance of intercellular calcium signaling in Drosophila wing development. *bioRxiv* https://doi.org/10.1101/187401.

29. Narciso, C. E., N. M. Contento, …, J. J. Zartman. 2017. Release of applied mechanical loading stimulates intercellular calcium waves in Drosophila wing discs. *Biophys. J.* 113:491–501.

30. Marada, S., D. P. Stewart, …, S. K. Ogden. 2013. The unfolded protein response selectively targets active smoothened mutants. *Mol. Cell. Biol.* 33:2375–2387.

31. Buchmann, A., M. Alber, and J. J. Zartman. 2014. Sizing it up: the mechanical feedback hypothesis of organ growth regulation. *Semin. Cell Dev. Biol.* 35:73–81.

32. Diaz de la Loza, M. C., and B. J. Thompson. 2017. Forces shaping the Drosophila wing. *Mech. Dev.* 144:23–32.

33. Hafen, E., and H. Stocker. 2003. How are the sizes of cells, organs, and bodies controlled? *PLoS Biol.* 1:E86.

34. Hariharan, I. K. 2015. Organ size control: lessons from Drosophila. *Dev. Cell.* 34:255–265.

35. Restrepo, S., J. J. Zartman, and K. Basler. 2014. Coordination of patterning and growth by the morphogen DPP. *Curr. Biol.* 24:R245–R255.

36. Narciso, C., and J. Zartman. 2018. Reverse-engineering organogenesis through feedback loops between model systems. *Curr. Opin. Biotechnol.* 52:1–8.

37. Duffy, J. B. 2002. GAL4 system in Drosophila: a fly geneticist's Swiss army knife. *Genesis.* 34:1–15.

38. Basler, K., and G. Struhl. 1994. Compartment boundaries and the control of Drosophila limb pattern by hedgehog protein. *Nature.* 368:208–214.

39. Nellen, D., R. Burke, …, K. Basler. 1996. Direct and long-range action of a DPP morphogen gradient. *Cell.* 85:357–368.

40. Strigini, M., and S. M. Cohen. 2000. Wingless gradient formation in the Drosophila wing. *Curr. Biol.* 10:293–300.

41. Mathews, J., and M. Levin. 2017. Gap junctional signaling in pattern regulation: physiological network connectivity instructs growth and form. *Dev. Neurobiol.* 77:643–673.

42. Badura, A., X. R. Sun, …, S. S. Wang. 2014. Fast calcium sensor proteins for monitoring neural activity. *Neurophotonics.* 1:025008.

43. Zartman, J., S. Restrepo, and K. Basler. 2013. A high-throughput template for optimizing Drosophila organ culture with response-surface methods. *Development.* 140:667–674.

44. Burnette, M., T. Brito-Robinson, …, J. Zartman. 2014. An inverse small molecule screen to design a chemically defined medium supporting long-term growth of Drosophila cell lines. *Mol. Biosyst.* 10:2713–2723.

45. Schindelin, J., I. Arganda-Carreras, …, A. Cardona. 2012. Fiji: an open-source platform for biological-image analysis. *Nat. Methods.* 9:676–682.

46. Liang, P., J. Chen, …, D. Z. Chen. 2018. A new registration approach for dynamic analysis of calcium signals in organs. *In* 2018 IEEE 15th International Symposium on Biomedical Imaging (ISBI 2018). Institute of Electrical and Electronic Engineers, pp. 934–937.

47. Capdevila, J., and I. Guerrero. 1994. Targeted expression of the signaling molecule decapentaplegic induces pattern duplications and growth alterations in Drosophila wings. *EMBO J.* 13:4459–4468.

48. Mirth, C. K., J. W. Truman, and L. M. Riddiford. 2009. The ecdysone receptor controls the post-critical weight switch to nutrition-independent differentiation in *Drosophila* wing imaginal discs. *Development.* 136:2345–2353.

49. Graveley, B. R., A. N. Brooks, …, S. E. Celniker. 2011. The developmental transcriptome of Drosophila melanogaster. *Nature.* 471:473–479.

50. Pézier, A. P., S. H. Jezzini, …, J. M. Blagburn. 2016. Shaking B mediates synaptic coupling between auditory sensory neurons and the giant fiber of Drosophila melanogaster. *PLoS One.* 11:e0152211.

51. Eid, J. P., A. M. Arias, …, M. Dziadek. 2008. The Drosophila STIM1 orthologue, dSTIM, has roles in cell fate specification and tissue patterning. *BMC Dev. Biol.* 8:104.

52. Fukami, K., S. Inanobe, …, Y. Nakamura. 2010. Phospholipase C is a key enzyme regulating intracellular calcium and modulating the phosphoinositide balance. *Prog. Lipid Res.* 49:429–437.

53. Murillo-Maldonado, J. M., F. B. Zeineddine, …, J. R. Riesgo-Escovar. 2011. Insulin receptor-mediated signaling via phospholipase C-γ regulates growth and differentiation in Drosophila. *PLoS One.* 6:e28067.

54. Johnston, L. A., and P. Gallant. 2002. Control of growth and organ size in Drosophila. *BioEssays.* 24:54–64.

55. Schaffter, T. 2014. From genes to organisms: Bioinformatics system models and software. PhD thesis. Ecole Polytechnique Fédérale de Lausanne.

56. Dahmann, C., A. C. Oates, and M. Brand. 2011. Boundary formation and maintenance in tissue development. *Nat. Rev. Genet.* 12:43–55.

57. Ayers, K. L., and P. P. Thérond. 2010. Evaluating smoothened as a G-protein-coupled receptor for hedgehog signalling. *Trends Cell Biol.* 20:287–298.

58. Alcedo, J., M. Ayzenzon, …, J. E. Hooper. 1996. The Drosophila smoothened gene encodes a seven-pass membrane protein, a putative receptor for the hedgehog signal. *Cell.* 86:221–232.

59. Tanimoto, H., S. Itoh, …, T. Tabata. 2000. Hedgehog creates a gradient of DPP activity in Drosophila wing imaginal discs. *Mol. Cell.* 5:59–71.

60. Box, G. E. P., and D. R. Cox. 1964. An analysis of transformations. *J. R. Stat. Soc. B.* 26:211–252.

61. Lecuit, T., W. J. Brook, …, S. M. Cohen. 1996. Two distinct mechanisms for long-range patterning by Decapentaplegic in the Drosophila wing. *Nature.* 381:387–393.

62. Wieser, R., J. L. Wrana, and J. Massagué. 1995. GS domain mutations that constitutively activate T beta R-I, the downstream signaling component in the TGF-beta receptor complex. *EMBO J.* 14:2199–2208.

63. Goberdhan, D. C., N. Paricio, …, C. Wilson. 1999. Drosophila tumor suppressor PTEN controls cell size and number by antagonizing the Chico/PI3-kinase signaling pathway. *Genes Dev.* 13:3244–3258.

64. Oldham, S., H. Stocker, …, E. Hafen. 2002. The Drosophila insulin/IGF receptor controls growth and size by modulating PtdInsP(3) levels. *Development.* 129:4103–4109.

65. Gao, X., T. P. Neufeld, and D. Pan. 2000. Drosophila PTEN regulates cell growth and proliferation through PI3K-dependent and -independent pathways. *Dev. Biol.* 221:404–418.

66. Hackley, C. R., E. O. Mazzoni, and J. Blau. 2018. cAMPr: a single-wavelength fluorescent sensor for cyclic AMP. *Sci. Signal.* 11: eaah3738.

67. Pan, Y., H. Alégot, …, K. D. Irvine. 2018. The dynamics of Hippo signaling during *Drosophila* wing development. *Development.* 145:dev165712.

68. Dye, N. A., M. Popović, …, S. Eaton. 2017. Cell dynamics underlying oriented growth of the *Drosophila* wing imaginal disc. *Development.* 144:4406–4421.

69. West, G. B., and J. H. Brown. 2005. The origin of allometric scaling laws in biology from genomes to ecosystems: towards a quantitative unifying theory of biological structure and organization. *J. Exp. Biol.* 208:1575–1592.

70. West, G. B., J. H. Brown, and B. J. Enquist. 1997. A general model for the origin of allometric scaling laws in biology. *Science.* 276:122–126.

71. Martín, F. A., and G. Morata. 2006. Compartments and the control of growth in the Drosophila wing imaginal disc. *Development.* 133: 4421–4426.

72. Praktiknjo, S. D., F. Saad, …, D. R. Hipfner. 2018. Activation of Smoothened in the Hedgehog pathway unexpectedly increases $G\alpha_s$-dependent cAMP levels in *Drosophila*. *J. Biol. Chem.* 293:13496–13508.

73. Hofer, A. M. 2012. Interactions between calcium and cAMP signaling. *Curr. Med. Chem.* 19:5768–5773.

74. Klatt Shaw, D., D. Gunther, …, D. J. Grunwald. 2018. Intracellular calcium mobilization is required for sonic hedgehog signaling. *Dev. Cell.* 45:512–525.e5.

75. Loew, L. M. 2007. Where does all the PIP2 come from? *J. Physiol.* 582:945–951.

76. Xu, C., J. Watras, and L. M. Loew. 2003. Kinetic analysis of receptor-activated phosphoinositide turnover. *J. Cell Biol.* 161:779–791.

77. Vinayagam, A., M. M. Kulkarni, …, N. Perrimon. 2016. An integrative analysis of the InR/PI3K/Akt network identifies the dynamic response to insulin signaling. *Cell Rep.* 16:3062–3074.

78. Martín-Castellanos, C., and B. A. Edgar. 2002. A characterization of the effects of Dpp signaling on cell growth and proliferation in the Drosophila wing. *Development.* 129:1003–1013.

79. Baumgartner, R., I. Poernbacher, …, H. Stocker. 2010. The WW domain protein Kibra acts upstream of Hippo in Drosophila. *Dev. Cell.* 18:309–316.

80. Genevet, A., M. C. Wehr, …, N. Tapon. 2010. Kibra is a regulator of the Salvador/Warts/Hippo signaling network. *Dev. Cell.* 18:300–308.

81. Yu, J., Y. Zheng, …, D. Pan. 2010. Kibra functions as a tumor suppressor protein that regulates Hippo signaling in conjunction with Merlin and Expanded. *Dev. Cell.* 18:288–299.

82. Finn, R. D., T. K. Attwood, …, A. L. Mitchell. 2017. InterPro in 2017-beyond protein family and domain annotations. *Nucleic Acids Res.* 45:D190–D199.

83. Weir, M. P., and C. W. Lo. 1982. Gap junctional communication compartments in the Drosophila wing disk. *Proc. Natl. Acad. Sci. USA.* 79:3232–3235.

84. Levin, M. 2007. Gap junctional communication in morphogenesis. *Prog. Biophys. Mol. Biol.* 94:186–206.

85. Richard, M., and M. Hoch. 2015. Drosophila eye size is determined by Innexin 2-dependent decapentaplegic signalling. *Dev. Biol.* 408:26–40.

86. Hoptak-Solga, A. D., K. A. Klein, …, M. K. Iovine. 2007. Zebrafish short fin mutations in connexin43 lead to aberrant gap junctional intercellular communication. *FEBS Lett.* 581:3297–3302.

87. Sahu, A., R. Ghosh, …, M. Prasad. 2017. A gap junction protein, Inx2, modulates calcium flux to specify border cell fate during Drosophila oogenesis. *PLoS Genet.* 13:e1006542.

88. Ralston, A., and S. S. Blair. 2005. Long-range Dpp signaling is regulated to restrict BMP signaling to a crossvein competent zone. *Dev. Biol.* 280:187–200.

89. Milán, M., F. J. Diaz-Benjumea, and S. M. Cohen. 1998. Beadex encodes an LMO protein that regulates Apterous LIM-homeodomain activity in Drosophila wing development: a model for LMO oncogene function. *Genes Dev.* 12:2912–2920.

90. Fletcher, A. G., M. Osterfield, …, S. Y. Shvartsman. 2014. Vertex models of epithelial morphogenesis. *Biophys. J.* 106:2291–2304.

91. Aegerter-Wilmsen, T., M. B. Heimlicher, …, K. Basler. 2012. Integrating force-sensing and signaling pathways in a model for the regulation of wing imaginal disc size. *Development.* 139:3221–3231.

92. Kursawe, J., P. A. Brodskiy, …, A. G. Fletcher. 2015. Capabilities and limitations of tissue size control through passive mechanical forces. *PLoS Comput. Biol.* 11:e1004679.

93. Nematbakhsh, A., W. Sun, …, M. Alber. 2017. Multi-scale computational study of the mechanical regulation of cell mitotic rounding in epithelia. *PLoS Comput. Biol.* 13:e1005533.

94. Barrack, D. S., R. Thul, and M. R. Owen. 2015. Modelling cell cycle synchronisation in networks of coupled radial glial cells. *J. Theor. Biol.* 377:85–97.

95. Barrack, D. S., R. Thul, and M. R. Owen. 2014. Modelling the coupling between intracellular calcium release and the cell cycle during cortical brain development. *J. Theor. Biol.* 347:17–32.

Biophysical Journal, Volume *116*

Supplemental Information

Decoding Calcium Signaling Dynamics during *Drosophila* Wing Disc Development

Pavel A. Brodskiy, Qinfeng Wu, Dharsan K. Soundarrajan, Francisco J. Huizar, Jianxu Chen, Peixian Liang, Cody Narciso, Megan K. Levis, Ninfamaria Arredondo-Walsh, Danny Z. Chen, and Jeremiah J. Zartman

Supplemental information for:
Decoding calcium signaling dynamics during *Drosophila* wing disc development

Pavel A. Brodskiy[1,†], Qinfeng Wu[1,†], Dharsan K. Soundarrajan[1], Francisco J. Huizar[1], Jianxu Chen[2], Peixian Liang[2], Cody Narciso[1], Megan K. Levis[1], Ninfamaria Arredondo-Walsh[1], Danny Z. Chen[2], and Jeremiah J. Zartman[1,*]

[1] Department of Chemical and Biomolecular Engineering, University of Notre Dame, Notre Dame, Indiana, 46556, USA
[2] Department of Computer Science and Engineering, University of Notre Dame, Notre Dame, Indiana, 46556, USA

[†] These authors contributed equally to this work
[*] Corresponding author

Supplemental material and methods

Fly strains and genetics

Unless otherwise indicated, stocks were obtained from Bloomington *Drosophila* Stock Center as indicated by stock number (BL#). Progeny wing phenotypes are from F1 male progeny emerging from the nub-Gal4, UAS-GCaMP6f/CyO x UAS-X cross. Representative results are summarized in Table S3. Male progenies were selected to avoid variation in wing size due to sex. The tester line (w1118; nubbin-GAL4, UAS-GCaMP6f/CyO) was generated as previously described (29). Flies were raised at 25 °C and 12-hour light cycle. When possible, we also performed multiple RNAi tests and selected the most severe phenotype for additional analysis. For perturbations to morphogenetic signaling, RNAi line phenotypes were consistent with loss-of-function phenotypes for target genes (Figure S7).

Fly extract preparation

One-gram well-nourished mature flies were homogenized in a tissue homogenizer (15 ml capacity, 0-1 mm clearance) with 6.82 ml of ZB media. Some fly extract was also ordered from Drosophila Genomics Resource Center. This homogenate was centrifuged at 2600 rpm for 20 min at 4°C. The supernatant and the oily film above it were removed and heat-treated at 60°C for 20 min. This preparation was then spun at 2600 rpm for 90 min at 4°C. The supernatant (fly extract) was removed, sterilized by 0.2 µm filtration, and stored at 4°C.

Wing disc imaging setup

We used two methods to culture the wing disc for imaging:

Culture method 1 is a modification of the procedure described in (42): We truncated the legs of a cell culture insert (EDM Millipore).” We then put the insert on top of a pool of pool of media to immobilize the wing discs. 50 µL of embryo oil was added along the outer periphery of the insert to seal. 100 µL of organ culture media was added on top of membrane of the insert (42).

Culture method 2 is described in (29), which reduced organ motion compared to method 1.

Imaging was performed on a Nikon Eclipse T*i* confocal microscope (Nikon Instruments, Melville, NY) with a Yokogawa spinning disc and MicroPoint laser ablation system (Andor Technology, South Windsor, CT). Image data were collected on an iXonEM+ cooled CCD camera (Andor Technology, South Windsor, CT) using MetaMorph® v7.7.9 software (Molecular Devices, Sunnyvale, CA). We found that the GCaMP6f sensor saturated at 80% laser intensity, but that intensity was linearly related at values under 70% (Fig. S5). Image intensity was linearly normalized to be comparable at 50% laser intensity.

Identification of the axes

Each image was presented as a 2x2 grid of the image either not transformed, flipped left/right, flipped top/down, or rotated 180 degrees in random order. The user selected the correctly-oriented pouch. The order in which the pouches were displayed was randomized, and a consensus was reached once three guesses were made if all three were the same. 77% of the samples were unambiguously classified in the first attempt in this way. If the first three guesses were not the same, then when more than half of the guesses were the same orientation, the most common orientation was taken to be the consensus. Two images were removed from the analysis because no consensus was reached after seven attempts.

Feature extraction

Each signal was decomposed into the following features: amplitude, frequency and integrated intensity, which comprise the Ca^{2+} signature of the ROI. Amplitude is defined as the mean of the amplitudes of the peaks, where the amplitude of each peak is the prominence of the peak in the *findpeaks* algorithm. F (mHz) is the number of peaks detected divided by the length of the signal in time (Fig. 6C, Fig. S1D-E). The integrated intensity (a.u.) is the time-averaged integral of the signal over time using a trapezoidal approximation.

The normalized intensity ($\Delta I(t)/I_o$) was approximated by using a bandpass Gaussian filter, where the larger sigma value adjusted for change in basal level over time, and the smaller sigma value compensated for stochastic noise. Spikes in signaling activity were extracted from $\Delta I(t)/I_0$ using the MATLAB *findpeaks* algorithm, with a minimum amplitude (Amp_{min}) and refractory period. MATLAB's genetic algorithm *ga* was used to calibrate the feature extraction parameters (Fig. 6C, Fig. S3, Table S4). To generate reference values for optimization of feature extraction parameters, 233 signals (I(t)) were randomly selected from 656,000 total signals, and manually annotated to identify the times (t_1 and t_2) at which each peak begins and ends. From this, the basal level was taken to be:

$$B_{manual} = \min\big(I(t\epsilon[t_1, t_2])\big)$$

the amplitude was extracted, as equal to:

$$Amp_{manual} = \max\big(I(t\epsilon[t_1, t_2])\big) - B_{manual}$$

and the width at half max (WHM) was taken to be the total time that the signal was greater than the average of the amplitude:

$$\mathrm{WHM}_{manual} = \mathrm{sum}\left(I(t\epsilon[t_1, t_2]) > \frac{(Amp_{manual} - B_{manual})}{2}\right)$$

The genetic algorithm was run at default settings for 172 generations. The objective function Err_1 was the sum of the squared differences of the correlation coefficients of the manual measurements and automatic measurements normalized to manual measurements. Err_2 was the fraction of signals with no waves incorrectly selected to contain waves compared to the manual ground-truth annotated data:

$$Err_1 = \sqrt{\left(\frac{Amp_{manual} - Amp_{auto}}{Amp_{manual}}\right)^2 + \left(\frac{WHM_{manual} - WHM_{auto}}{WHM_{manual}}\right)^2 + \left(\frac{B_{manual} - B_{auto}}{B_{manual}}\right)^2}$$

$$Err_2 = \frac{1}{N}\sum_{i}^{N}(WHM_{manual} = 0 \,\&\, WHM_{auto} > 0)$$

where N is the number of signals analyzed (N = 233). A Pareto front was generated to demonstrate the trade-offs between summary statistic error and false positives. Parameter values were selected that minimized both measurement error and false positives (Fig. S3, Table S4).

Statistical analysis and visualization

To compare across compartments, medians were taken after dividing discs into A compartment and P compartment such that the A-P compartment boundary was approximated with a vertical line fitted to points along the A/P axis. A two-tailed, paired Student's t-test was performed. The F-test for model fit relative to a constant model was used to determine whether each summary statistic was related to pouch size. As outlined in Fig. 6, spatial maps were generated for each wing disc to explore the impact of spatial position, developmental progression, and genetic perturbations on Ca^{2+} signatures. The composite maps in Fig. 7 represent the consensus of multiple wing discs from each condition. These spatial composites were mapped to a canonical described in (52) (Fig. S4)

Qualitative analysis

Qualitative analysis was reported in Fig. 3F,G, 5E,F, and 7C. Each bar represents the overall fraction of time discs undergo each class of signaling. Each measurement indicates a class assigned to an individual video clip, and each measurement was weighted equally. nub-GCaMP6 serves as controls. nub-GCaMP6 represents measurements taken from wandering larvae. Results of proportions test for Fig. 5F and 7C are summarized in Table S6 and S7. Analysis for Fig. 3F,G, and 5E,F was performed using an ordinal regression to determine whether pouch size significantly impacts the class of Ca^{2+} activity. This analysis assumes a hierarchy of activity with no activity being the least active category and "fluttering" being the most active category. This hierarchy activity is established based the FEX dose-response experiments in Fig. 3.

Experimental limitations

It can be noted that a possible limitation of the present study is the use of the GCaMP6f-based reporters to visualize Ca^{2+} signaling activity. For example, certain levels of Ca^{2+} might be out of the range of detection of the GCaMP6f sensor. It may be possible that a different Ca^{2+} sensor with a different affinity to Ca^{2+} may report different Ca^{2+} dynamics. Further, we cannot rule out the

possibility that genetic perturbations might impact total levels of GCaMP6f expression under the nub-Gal4 driver. This can be addressed in future studies by systematic ratiometric measurements of Ca^{2+} such as normalizing to mCherry expression and by comparing additional readouts of calcium signaling as new techniques are developed.

Index of Supplementary Figures:

Figure S1: Signal extraction from wing discs

Figure S2: Manual identification of the wing disc pouch orientation

Figure S3: Optimization of image analysis parameters

Figure S4: Transformation of spatial maps onto a canonical axis

Figure S5: Correlation of laser power with image intensity

Figure S6: Normalized and unnormalized integrated intensities are highly correlated

Figure S7: Evaluation of linear, exponential, and power models for intensity vs. pouch size

Figure S8: Representative wing phenotypes from the MS1096 crosses used in this study

Figure S9: Representative wing phenotypes from the nub-GAL4>GCaMP6f crosses used in this study

Figure S10: Multiple Smo RNAi lines all abolish the anterior-posterior patterning of amplitude as shown in these composites.

Figure S11: Quantification of anterior and posterior vein defects with various RNAi knockdowns

Table S1: Line validation details

Table S2: *Drosophila* lines

Table S3: MS1096-Gal4>UAS-RNAi phenotype summary

Table S4: Parameters of feature extraction pipeline

Table S5: Extended data movies

Table S6: Qualitative proportion p-values

Table S7: Qualitative proportion raw values

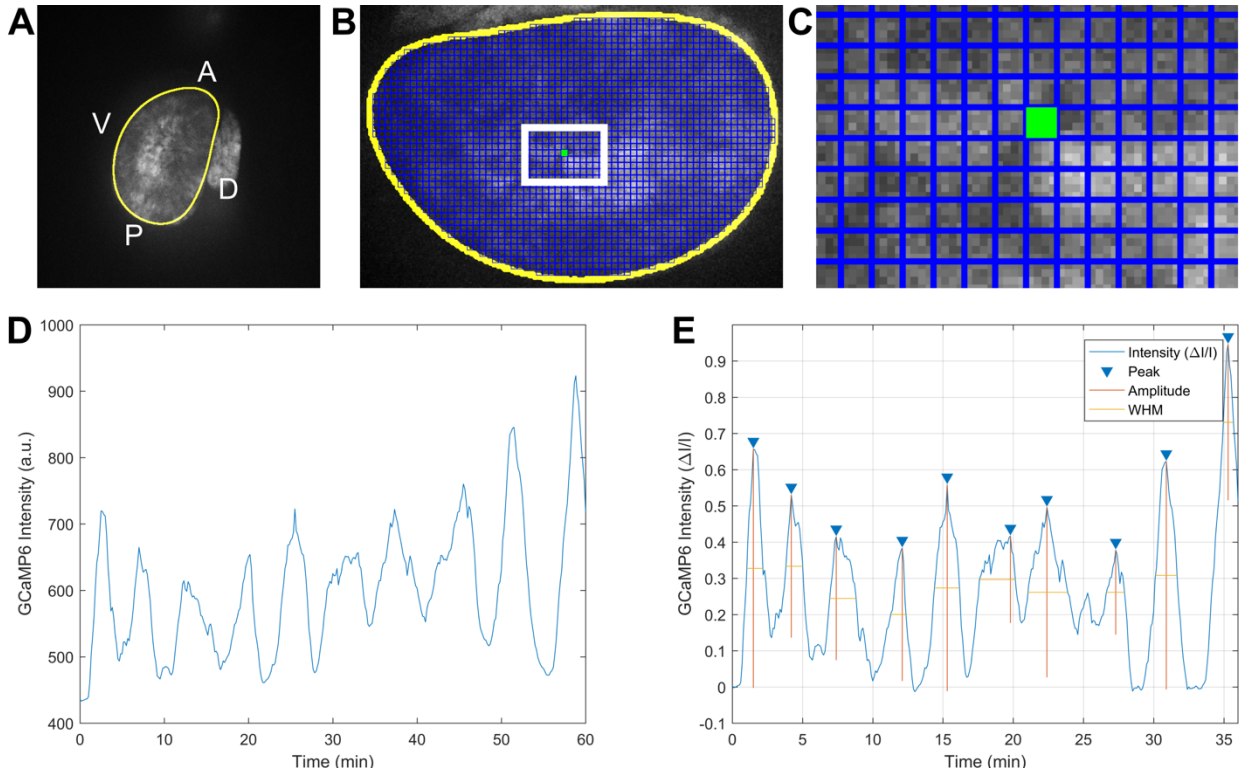

Figure S1: Signal extraction from wing discs

(A) Maximum intensity Z-projection of one frame of time-lapse video. (B) Manual mask around pouch, and grid of square regions of interest (ROIs). (C) Individual ROI is averaged over space to obtain a one-dimensional intensity profile. (D) Raw intensity profile. (E) Normalized intensity profile with amplitudes and widths at half max (WHM) marked.

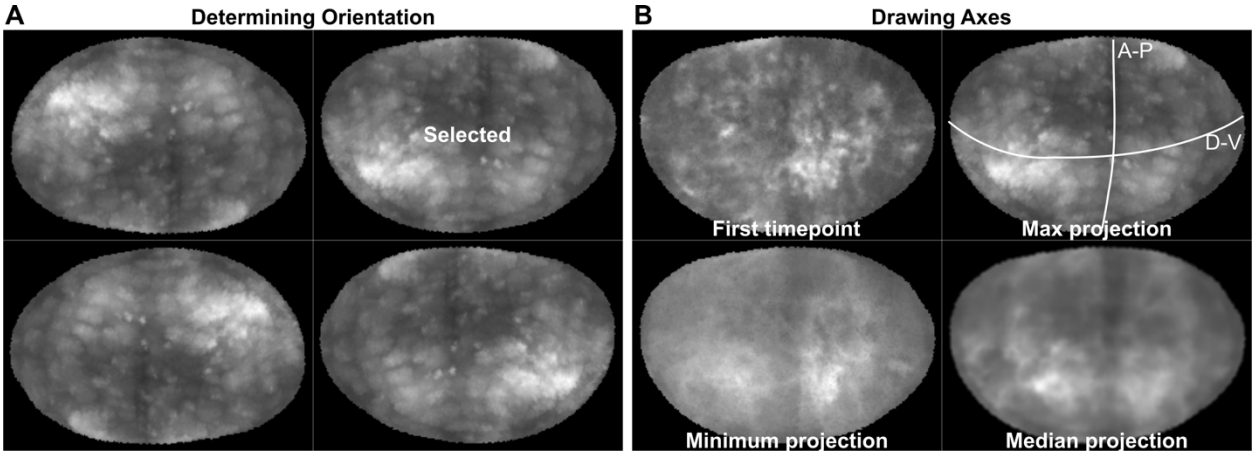

Figure S2: Manual identification of the wing disc pouch orientation

(A) Workflow for manual selection of orientation. Registered time stack was max projected over time in FIJI. The maximum projection was shown in a 2 x 2 format to the user with a non-processed, horizontally-flipped, vertically-flipped, and 180-degree rotated image presented in a random order. The user selected the image with the P compartment on the right and the D compartment on the top. Based on size and orientation, landmarks used to make the classification include the shape and size of the compartments as indicated in Fig. 1B. The pouches were presented in a random order and were repeated at least three times. If all three initial classifications were the same, that orientation was taken to be the consensus. If more than three attempts were needed, a consensus was reached when more than half of the selected discs were the same orientation. Two discs did not reach a consensus orientation after seven attempts and were not included in the analysis. (B) Workflow for axes selection. The first timepoint, max projection, min projection, and median projection were shown to the user in a 2x2 format. Curves were drawn for the A-P and D-V axes. The A-P axis generally aligns with a sharp decrease in intensity on the maximum projection, and the D-V axis generally aligns with an increase in basal level on the minimum projection. White lines indicate manual annotations of axes.

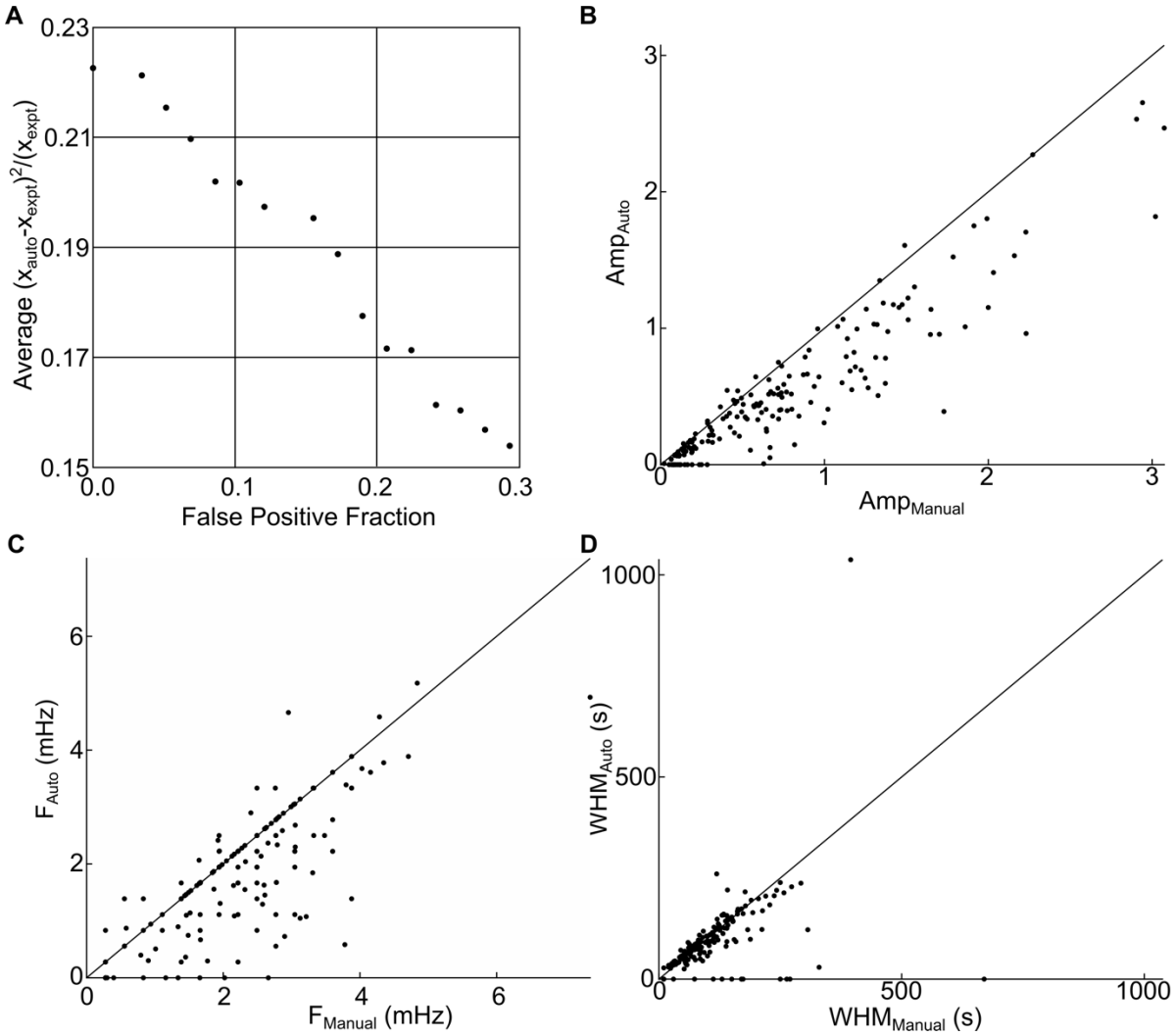

Figure S3: Optimization of image analysis parameters

(A) Pareto optimization chart for final solution. b-d, Comparison of automatically-extracted values and manually measured values for (B) frequency, (C) amplitude, and (D) time between peaks.

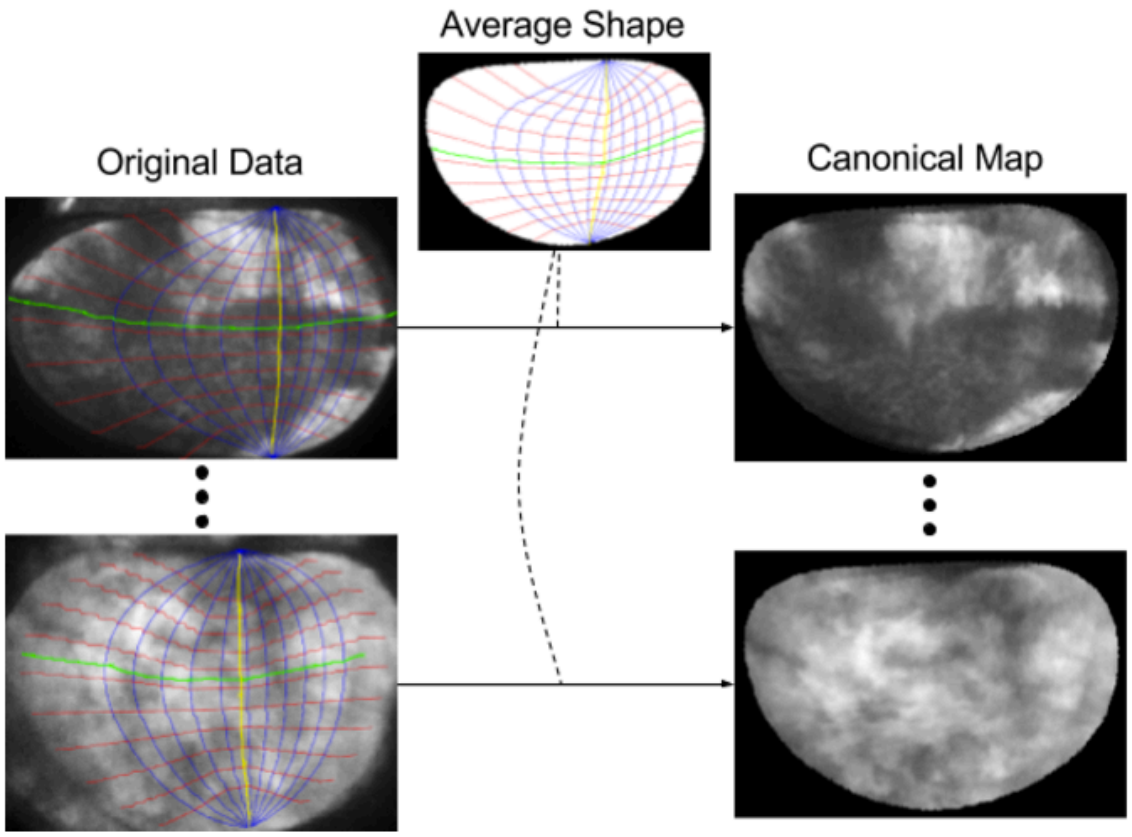

Figure S4: Transformation of spatial maps onto a canonical axis
A pouch coordinate system is defined along the A/P axis (the green curve) and the D/V axis (the yellow curve), similar to the latitude (cf. red curves) and longitude (cf. blue curves) of the geographic coordinate system. This coordinate system is constructed for each pouch. A mapping from the pouch coordinates in an input image to the corresponding pouch coordinates of the average shape transforms the original data to a canonical map.

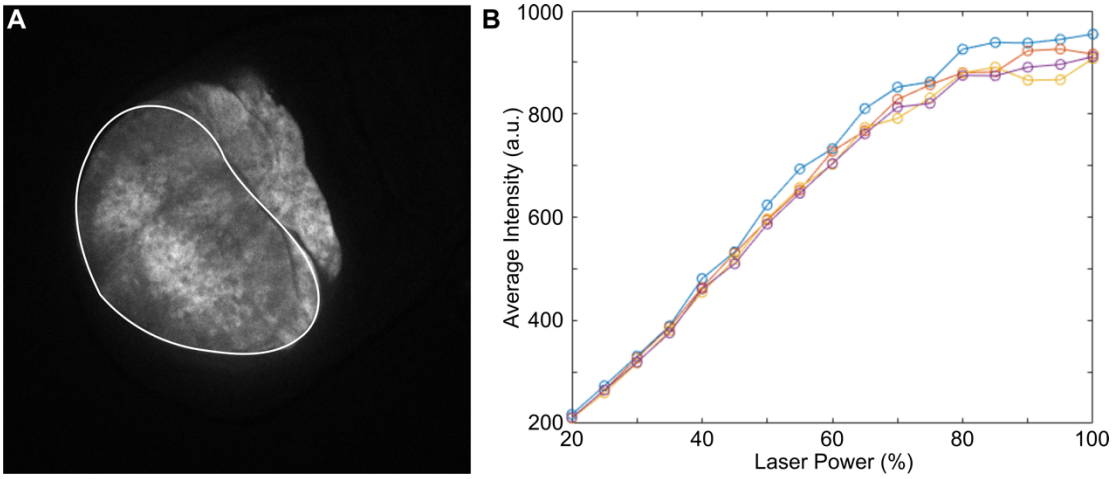

Figure S5: Correlation of laser power with image intensity

(A) Z-projection of confocal image of nub-GCaMP6f wing disc acquired at a laser power of 50% (n = 4). Pouch was segmented, and the average intensity of the pouch was obtained at various laser powers. (B) Average intensity of the pouch varies linearly with laser intensity under 80%.

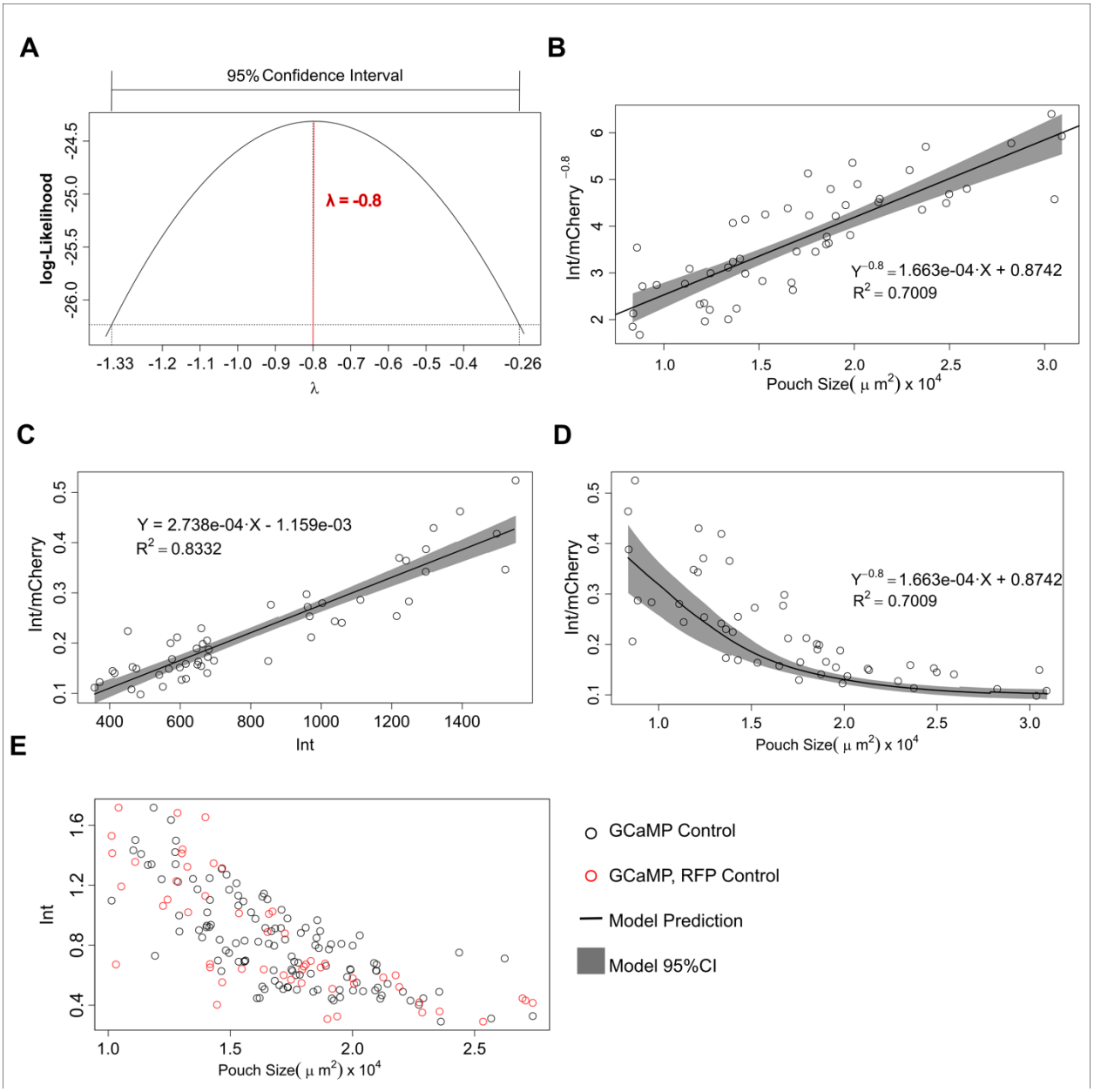

Figure S6: Normalized and unnormalized integrated intensities are highly correlated

A) Log-likelihood estimation of a parameter lambda to be used as an exponent in a power transformation of the data set. The maximum likelihood estimate of lambda was found to be -0.8 ± 0.53. This falls within the range of quarter-power scaling that has observed to occur in many biological contexts. B) Integrated intensity normalized to mCherry intensity is correlated to pouch size in a -0.80-power scaling fashion (R^2 = 0.70). Linear fit of power-transformed intensity from the log-likelihood estimation of λ. C) Normalized integrated intensity is correlated to unnormalized integrated intensity with a linear fit (R^2 = 0.83). D) Integrated intensity normalized to mCherry intensity with the back-transformed fit. E) Unnormalized integrated intensity for both nub-Gal4>UAS-GCaMP6f and nub-Gal4>UAS-GCaMP6f/ >UAS-mCherry. Justification of the power-scaling model is addressed in Fig. S7. CI: confidence interval.

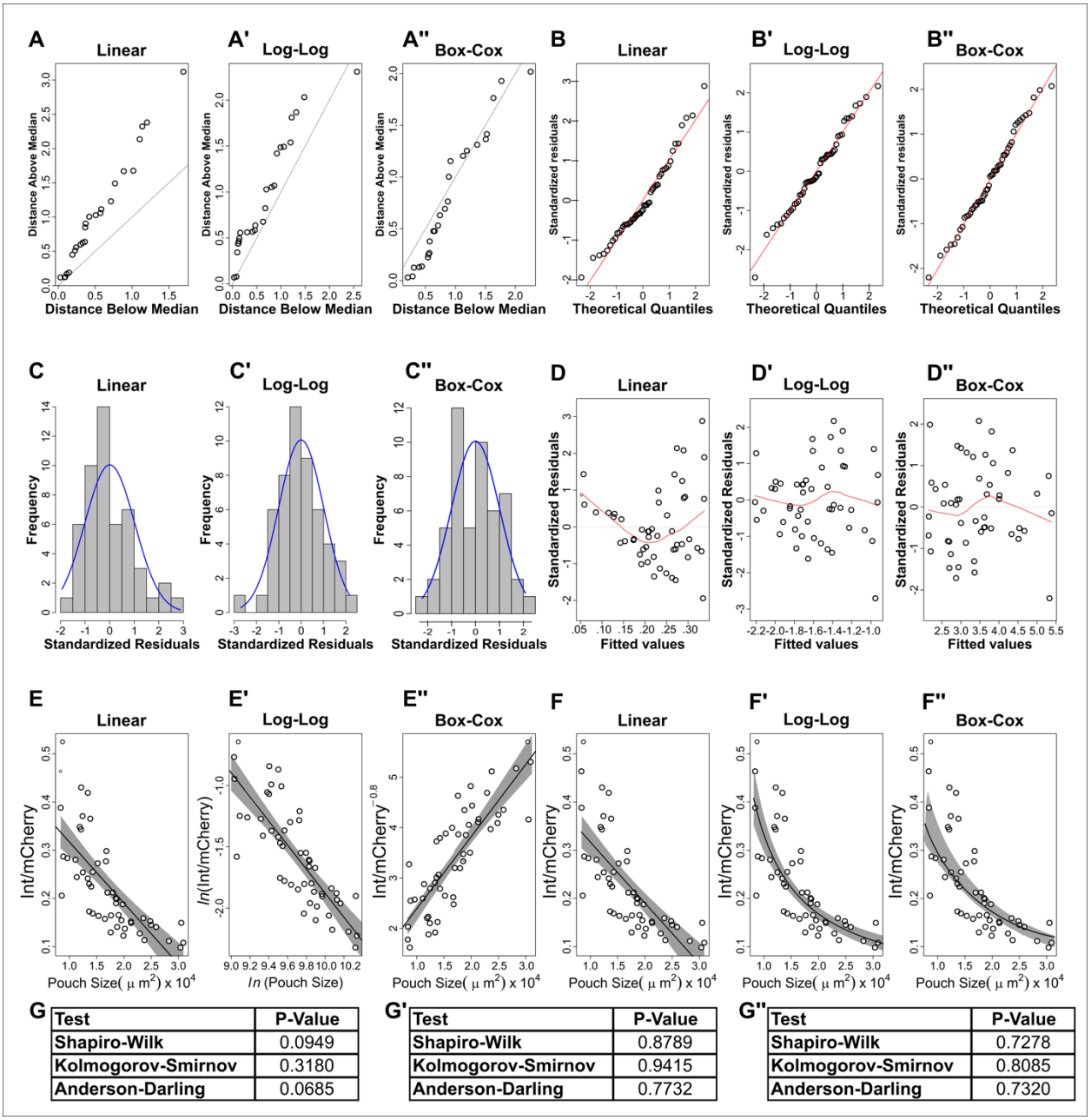

G

Test	P-Value
Shapiro-Wilk	0.0949
Kolmogorov-Smirnov	0.3180
Anderson-Darling	0.0685

G'

Test	P-Value
Shapiro-Wilk	0.8789
Kolmogorov-Smirnov	0.9415
Anderson-Darling	0.7732

G"

Test	P-Value
Shapiro-Wilk	0.7278
Kolmogorov-Smirnov	0.8085
Anderson-Darling	0.7320

Figure S7: Evaluation of linear, exponential, and power models for ratiometric (normalized) integrated intensity vs. pouch size

Comparison of regression models. A) Symmetry distributions of standardized residuals around the medians. Residuals are normally distributed if data on both sides of the median are equally distributed. Both linear and log-log transformed residuals show clear signs of asymmetry whereas the Box-Cox power-scaled transformation is evenly distributed around the median. B) Quantile-Quantile plots of the standardized residuals. If the residuals are from a normal distribution, they will lie on the red line that has an intercept equal to the mean of the residuals and a slope equal to the standard deviation. Linear model is heavily skewed while the log-log transformed model is slightly skewed to the left. Box-Cox power-scaled model has the best distribution along the red

line. C) Histograms of the standardized residuals with a blue superimposed normal curve. Residuals that are normally distributed should follow along the blue curve. The linear model residuals are heavily skewed while the log-log and power-scaled models have roughly normal distributions. D) Residuals versus fitted values of the standardized residuals. Residuals have constant variance if the values are centered around the dashed zero line. A red line is superimposed detailing the spread of the residuals. The linear model has non-constant variance in the residuals while the log-log model and power-scale model both have constant variance. E) Linear fits of each model to the untransformed data in the case of the linear model and the transformed data in the case of the log-log and power-scale model. The black line denotes the regression line and the surrounding grey bounds represent the 95% confidence interval of the regression line. F) Back-transformed fits of each model to untransformed data. G) Three normality tests were performed on the model residuals: Shapiro-Wilk, Kolmogorov-Smirnov, and Anderson-Darling. For the Shapiro-Wilk test, a p-value below 0.05 indicates there is evidence that the data tested are not from a normally distributed population. For the Kolmogorov-Smirnov normality test, a p-value closer to one provides evidence that the sample is drawn from a normal distribution. For the Anderson-Darling test, a p-value below 0.05 would indicate there is evidence that the data does not conform to a normal distribution. We concluded that a power-scaled model is reasonable with p-values > 0.05 for the normality tests, and the model had minimal variance and normally distributed residuals compared to the purely linear and log-transformed models.

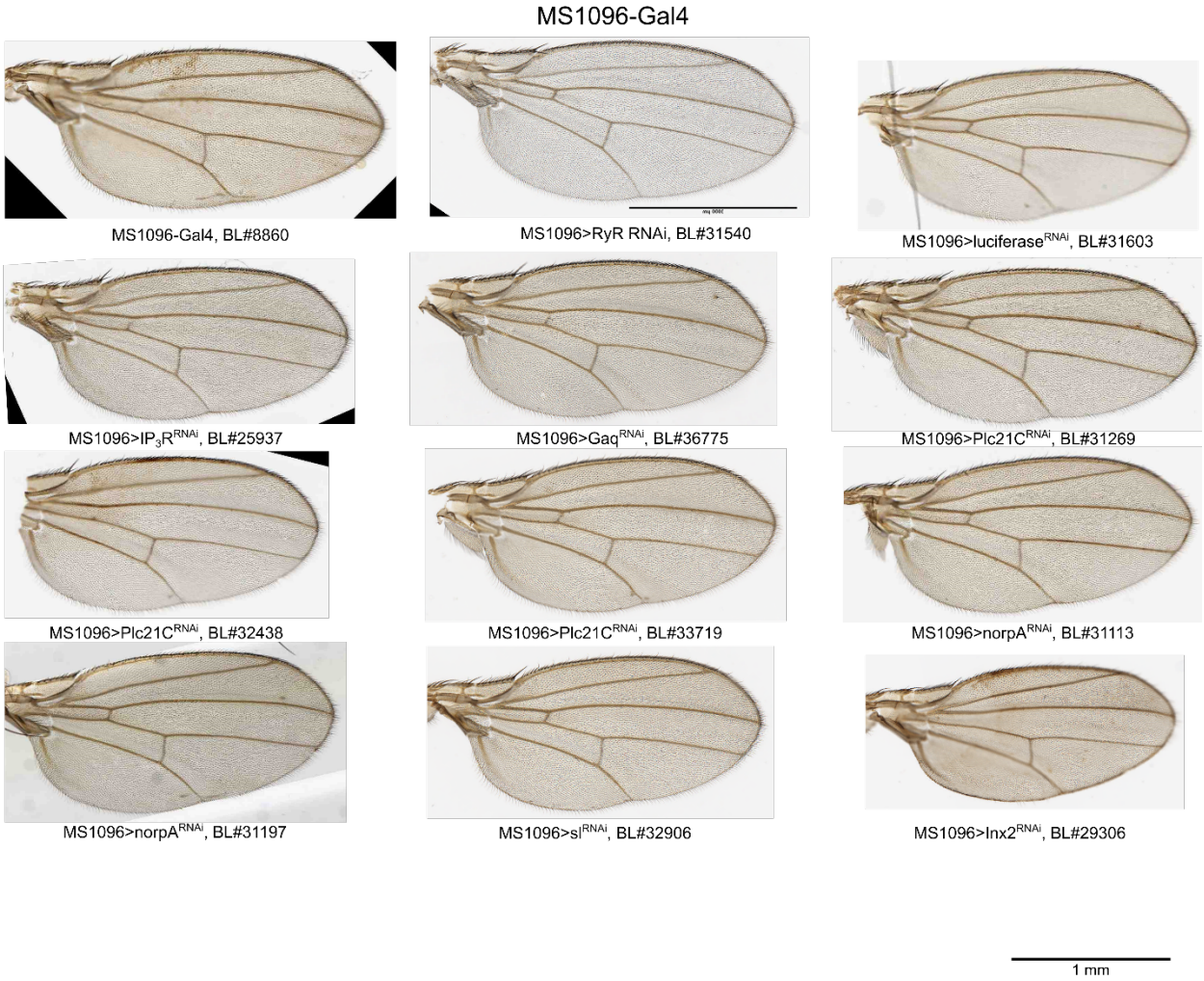

Figure S8: Representative wing phenotypes from the MS1096 crosses used in this study

The scale bar is 1 mm. For imaging the dorsal compartment specific MS1096-Gal4 driven crosses, the three-dimensional bending phenotype is obscured. Wing images were selected randomly from the sample of wings quantified in Fig. 2. The larval overgrowth phenotype generated by tkv^{CA} results in distorted wings.

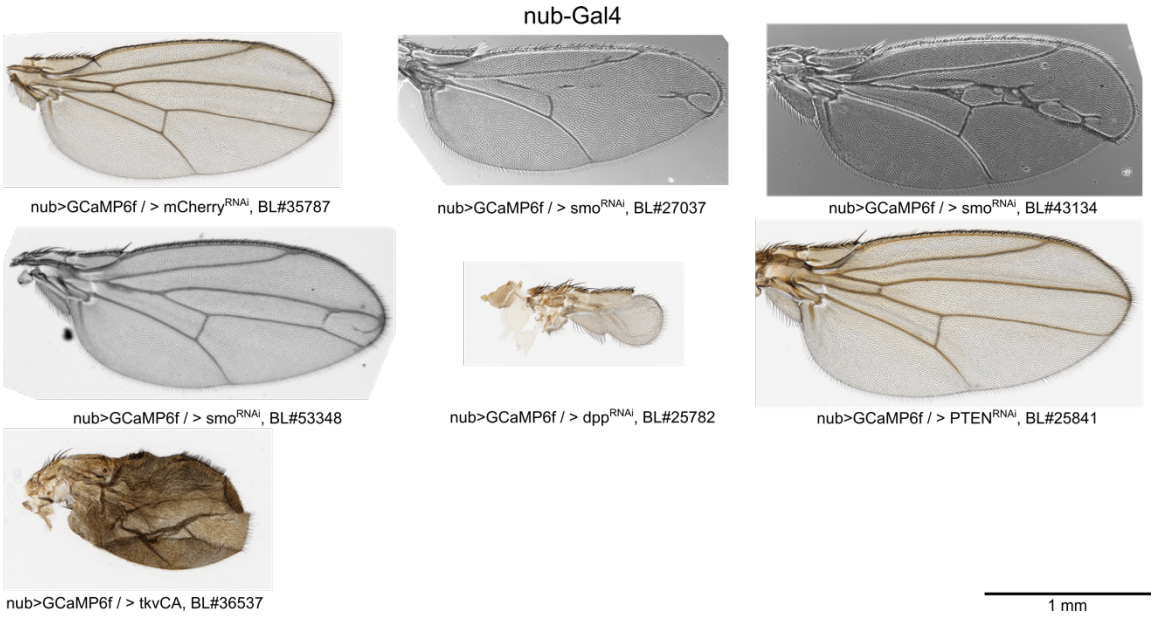

Figure S9: Representative wing phenotypes from the nub-GAL4>GCaMP6f crosses used in this study

The scale bar is 1 mm. To image Ca^{2+} dynamics in the wing disc pouch, we used nub-GAL4 to express genetically encoded Ca^{2+} sensor (GCaMP6f sensor). The larval overgrowth phenotype generated by tkv^{CA} results in distorted wings.

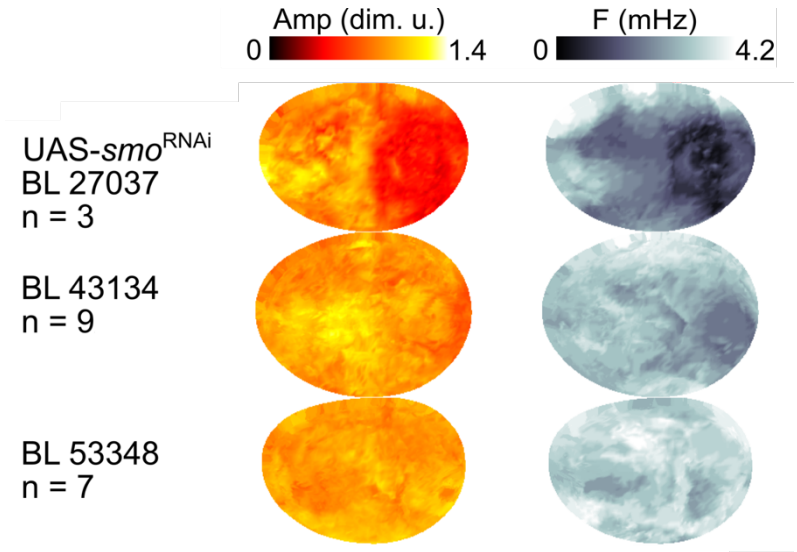

Figure S10: Multiple *Smo*^{RNAi} lines all abolish the anterior-posterior patterning of amplitude as shown in these composites.
For validation of RNAi knockdown strength refer to severity of wing phenotypes in Fig S9.

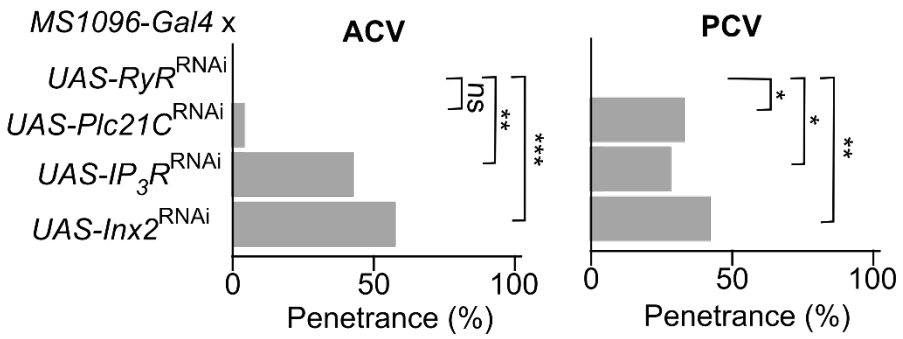

Figure S11: Quantification of anterior and posterior cross veins in various RNAi lines knockdowns.

ACV and PCV vein defects were observed when *RyR*, *Plc21C*, *IP3R* and *Inx2* genes were knocked down using *MS1096-GAL4* driver. ACV and PCV defects were quantified manually. Proportions test was performed, and the asterisks denote significance (* = $p < 0.05$, ** = $p < 0.01$, *** = $p < 0.001$, ns = not significant)

Table S1: Line validation details

Line	Condition	Validation
BL#25937	*UAS-IP3R^{RNAi}*	This RNAi line shows a documented wound healing phenotype described in (15), and epithelial folding defects described in (26)
BL#29306	*UAS-Inx2^{RNAi}*	This RNAi line shows a documented wound healing phenotype and phenocopies Ca^{2+} phenotype described in (15)
BL#42645	*UAS-Inx2^{RNAi}*	This RNAi line shows an auditory response phenotype documented in (93). This line shows qualitatively similar but weaker Ca^{2+} phenotypes compared to BL#29306
BL#27263	*UAS-SERCA^{RNAi}*	Wing phenotype in Fig. S8 matches SERCA^{RNAi} phenotypes of BL#24928 shown in supplementary Figure 5 of (15)
BL#25928	*UAS-SERCA^{RNAi}*	Wing phenotype in Fig. S8 matches SERCA^{RNAi} phenotypes of BL#24928 shown in supplementary Figure 5 of (15)
BL#31540	*RyR^{RNAi}*	The lack of a phenotype in the wing or observed calcium signaling dynamics suggests that RyR plays an insignificant role in wing development. No expression of RyR has been reported in the wing disc (94).

Table S2: *Drosophila* lines

Name	Source	Genotype
nub-Gal4, UAS-GCaMP6f	(29)	nub-GAL4, UAS-GCaMP6f/CyO, UAS-Dcr-2
MS1096-Gal4	BL#8860	w[1118] P{w[+mW.hs]=GawB}Bx[MS1096]
UAS-*dpp*^{RNAi}	BL#25782	y[1] v[1]; P{y[+t7.7] v[+t1.8]=TRiP.JF01371}attP2
UAS-*pten*^{RNAi}	BL#25841	y[1] v[1]; P{y[+t7.7] v[+t1.8]=TRiP.JF01859}attP2
UAS-IP3R^{RNAi}	BL#25937	y[1] v[1]; P{y[+t7.7] v[+t1.8]=TRiP.JF01957}attP2
UAS-*Inx2*^{RNAi}	BL#29306	y[1] v[1]; P{y[+t7.7] v[+t1.8]=TRiP.JF02446}attP2
UAS-norpA^{RNAi}	BL#31113	y[1] v[1]; P{y[+t7.7] v[+t1.8]=TRiP.JF01585}attP2
UAS-norpA^{RNAi}	BL#31197	y[1] v[1]; P{y[+t7.7] v[+t1.8]=TRiP.JF01713}attP2
UAS-Plc21C^{RNAi}	BL#31269	y[1] v[1]; P{y[+t7.7] v[+t1.8]=TRiP.JF01210}attP2
UAS-luciferace^{RNAi}	BL#31603	y[1] v[1]; P{y[+t7.7] v[+t1.8]=TRiP.JF01355}attP2
UAS-Plc21C^{RNAi}	BL#32438	y[1] sc[*] v[1]; P{y[+t7.7] v[+t1.8]=TRiP.HMS00436}attP2/TM3, Sb[1]
UAS-*sf*^{RNAi}	BL#32906	y[1] sc[*] v[1]; P{y[+t7.7] v[+t1.8]=TRiP.HMS00695}attP2
UAS-*dpp*^{RNAi}	BL#33618	y[1] v[1]; P{y[+t7.7] v[+t1.8]=TRiP.HMS00011}attP2
UAS-Plc21C^{RNAi}	BL#33719	y[1] sc[*] v[1]; P{y[+t7.7] v[+t1.8]=TRiP.HMS00600}attP2
UAS-tkv^{CA}	BL#36537	w[*]; P{w[+mC]=UAS-tkv.CA}3
UAS-Gaq^{RNAi}	BL#36775	y[1] v[1]; P{y[+t7.7] v[+t1.8]=TRiP.JF02390}attP2
UAS-*smo*^{RNAi}	BL#27037	y[1] v[1]; P{y[+t7.7] v[+t1.8]=TRiP.JF02363}attP2
UAS-*smo*^{RNAi}	BL#43134	y[1] v[1]; P{y[+t7.7] v[+t1.8]=TRiP.GL01472}attP2
UAS-*smo*^{RNAi}	BL#53348	y[1] sc[*] v[1]; P{y[+t7.7] v[+t1.8]=TRiP.HMC03577}attP40
UAS-mCherry	BL#35787	y[1] sc[*] v[1]; P{y[+t7.7] v[+t1.8]=UAS-mCherry.VALIUM10}attP2
UAS-*SERCA*^{RNAi}	BL#44581	y[1] sc[*] v[1]; P{y[+t7.7] v[+t1.8]=TRiP.HMS02878}attP2

Table S3: MS1096-Gal4>UAS-RNAi phenotype summary

Gene	Function	Phenotype
IP_3R	Releases Ca^{2+} from ER to cytosol	Bent wings, smaller, increases vein differentiation defects
Gαq	Produces PLCβ	Bent wings, smaller, vein differentiation
Inx2	Forms gap junctions	Bent wings, smaller, vein differentiation
SERCA	Pumps Ca^{2+} from cytosol to ER	Shriveled wings (strong)
norpA	PLCβ4 homolog, produces IP_3	Normal
Plc21C	PLCβ1 homolog, produces IP_3	Bent wings, vein differentiation defects
sl	PLCγ homolog, produces IP_3	Bent wings, smaller, vein differentiation

Table S4: Parameters of feature extraction pipeline

Parameter	Optimized Value	Meaning
Amp_{min}	0.29	Minimum peak amplitude
WHM_{min}	23 s	Minimum duration of peak
Refractory Period	10 s	Minimum time between peaks
σ_{min}	8 s	Parameter for high-frequency Gaussian filter for removing noise
σ_{max}	1100 s	Parameter for low-frequency Gaussian filter for adapting to changes in basal level

Table S5: Extended data movies

SI Movie #	Description
1	nub-Gal4>UAS-GCaMP6f, in vivo, spike
2	nub-Gal4>UAS-GCaMP6f, in vivo, ICT
3	nub-Gal4>UAS-GCaMP6f, in vivo, ICW
4	nub-Gal4>UAS-GCaMP6f, in vivo, fluttering
5	nub-G4>UAS-GCaMP6f/ UAS-IP_3R^{RNAi}, in vivo, BL# 25937
6	nub-G4>UAS-GCaMP6f/UAS-$SERCA^{RNAi}$, in vivo, BL# 44581
7	nub-G4>UAS-GCaMP6f/UAS-$Inx2^{RNAi}$, in vivo, BL# 29306
8	nub-G4>UAS-GCaMP6f/UAS-$Plc21C^{RNAi}$, in vivo, BL# 31269
9	nub-G4>UAS-GCaMP6f/UAS-$norpA^{RNAi}$, in vivo, BL# 31113
10	nub-G4>UAS-GCaMP6f/UAS-sl^{RNAi}, in vivo, BL# 32906
11	nub-G4>UAS-GCaMP6f/UAS-$G\alpha q^{RNAi}$, ex vivo, BL# 36775
12	nub-G4>UAS-GCaMP6f/UAS-IP_3R^{RNAi}, ex vivo, BL# 25937
13	nub-G4>UAS-GCaMP6f/UAS-$Plc21C^{RNAi}$, ex vivo, BL# 31269
14	nub-Gal4>UAS-GCaMP6f, in ZB media + 0% FEX
15	nub-Gal4>UAS-GCaMP6f, in ZB media + 2.5% FEX
16	nub-Gal4>UAS-GCaMP6f, in ZB media + 5% FEX
17	nub-Gal4>UAS-GCaMP6f, in ZB media + 10% FEX
18	nub-Gal4>UAS-GCaMP6f, in ZB media + 20% FEX
19	nub-Gal4>UAS-GCaMP6f, in ZB media + 40% FEX
20	nub-G4>UAS-GCaMP6f/UAS-$Inx2^{RNAi}$, ex vivo, BL# 29306
21	nub-G4>UAS-GCaMP6f/UAS-Smo^{RNAi}, ex vivo, BL# 43134
22	nub-G4>UAS-GCaMP6f/UAS-Dpp^{RNAi}, ex vivo, BL# 25782
23	nub-G4>UAS-GCaMP6f/UAS-$Pten^{RNAi}$, ex vivo, BL# 25841
24	nub-G4>UAS-GCaMP6f/UAS-mCherry, ex vivo, BL# 35787

FEX: fly extract

Table S6: Qualitative proportion p-values

Calculated categorical proportions for each tested knockdown are shown below. The proportion of each type of activity was compared with unperturbed *nub-Gal4>UAS-GCaMP6f* wandering larvae. We report p-values obtained from the proportion test. p-values under 0.05 are highlighted and considered significant. For example, all conditions show a difference in total activity except for *norpA*^{RNAi} and *sl*^{RNAi}; however, the *sl*^{RNAi} condition spends proportionally more time undergoing spike activity and less time undergoing waves and fluttering than the unperturbed control. Raw measurements are reported in Table S6. Bold highlights indicate significant differences (p-value < 0.05).

IP$_3$R^{RNAi}	**3.0E-03**	9.7E-01	4.2E-01	**2.6E-02**	**3.1E-02**
SERCA^{RNAi}	**9.5E-06**	3.3E-01	**2.8E-02**	**4.3E-03**	**3.9E-02**
Inx2^{RNAi}	**8.1E-50**	**3.2E-99**	4.0E-01	2.6E-01	5.3E-02
Gαq^{RNAi}	**1.3E-06**	3.1E-01	**6.7E-03**	**3.2E-03**	**3.3E-02**
Plc21C^{RNAi}	**9.3E-06**	3.8E-01	**6.5E-03**	**5.8E-03**	**7.3E-03**
norpA^{RNAi}	8.3E-01	8.9E-01	**9.5E-03**	1.5E-01	**2.2E-02**
sl^{RNAi}	4.7E-01	**5.3E-05**	**3.3E-03**	**7.8E-03**	**1.5E-02**
smo^{RNAi}	**4.5E-04**	9.7E-02	6.1E-01	**8.7E-07**	**3.8E-02**

Table S7: Qualitative proportion raw values for in vivo data

Control	0.87	0.01	0.04	0.05	0.03	790	103
IP$_3$R^{RNAi}	0.95	0.01	0.03	0.01	0.00	164	19
SERCA^{RNAi}	0.99	0.00	0.01	0.00	0.00	150	21
Inx2^{RNAi}	0.30	0.56	0.06	0.08	0.00	131	16
Gαq^{RNAi}	1.00	0.00	0.00	0.00	0.00	54	6
Plc21C^{RNAi}	0.97	0.01	0.01	0.01	0.00	253	36
norpA^{RNAi}	0.88	0.01	0.09	0.03	0.00	185	22
sl^{RNAi}	0.85	0.04	0.10	0.01	0.00	207	25
smo^{RNAi}	0.78	0.02	0.05	0.14	0.01	290	40

Control is the average of multiple days (day 5-8). Due to smaller available sample sizes, genetic perturbations are within a three-day egg laying window.